Atmospheric Density Reconstruction Using Satellite Orbit Tomography[1]

Michael A. Shoemaker,[2] Brendt Wohlberg,[3] and Josef Koller[4]

Los Alamos National Laboratory, Los Alamos, NM, 87545

Improved thermospheric neutral density models are required for the reduction of orbit prediction errors for satellites experiencing atmospheric drag. This research describes a new method to estimate density using a tomography-based approach, inspired by X-ray computed tomography from the medical imaging field. The change in specific mechanical energy of the orbit is used as the measurement, which is related to the integrated drag acceleration over the orbit. Using several such measurements from a number of satellites, one can estimate a spatially resolved multiplicative correction to an assumed density model. The problem considered here uses simulated measurements from 50 low-Earth orbit satellites and solves for the correction factor discretized over 324 grid elements spanning 300 to 500 km altitude. This ill-posed problem is solved using Tikhonov regularization, with the three-dimensional gradient as the regularization operator, resulting in a penalty on the spatial smoothness of the estimated density. Simulation results show that the true time-averaged density can be reconstructed to within approximately 10%, using only assumed ground-based tracking measurements separated over 12 hours.

Nomenclature

A	=	cross-sectional area, km^2
a	=	semimajor axis, km
$\mathbf{a}$	=	perturbing acceleration vector, km/s^2
$\mathcal{C}$	=	satellite trajectory
C_d	=	drag coefficient, unitless
D	=	discretized regularization operator
$\mathcal{E}$	=	specific mechanical energy, km^2/s^2
E	=	eccentric anomaly, rad
e	=	eccentricity, unitless
f	=	X-ray attenuation coefficient
$\mathcal{H}$	=	linear measurement matrix
H	=	scale height, km
h	=	summed kernel, km^2/s^3
i	=	satellite index
K	=	set of times in a given cell
k	=	discrete time index
I	=	X-ray intensity
M	=	number of satellites

[1] Accepted to AIAA Journal of Guidance, Control, and Dynamics, Oct. 2013.

[2]Postdoctoral Research Associate, Space Science and Applications (ISR-1), P.O. Box 1663, Mail Stop D466

[3]Scientist, Applied Mathematics and Plasma Physics (T-5), P.O. Box 1663.

[4]Deputy Group Leader, Space Science and Applications (ISR-1), P.O. Box 1663, Mail Stop D466

m	= mass, kg
N	= number of cells in grid
n	= cell index
P	= number of satellite points in a cell
p	= semilatus rectum, km
R	= Earth radius, km
$\mathbf{r}$	= position vector of satellite, km
r	= radial distance, km
r_a, r_p	= radius of apogee and perigee, km
$\mathbf{s}$	= vector of density model scale factors, unitless
s	= density model scale factor, unitless
T	= specific kinetic energy, $\mathrm{km}^2/\mathrm{s}^2$
t	= time, s
U	= specific gravitational potential energy, $\mathrm{km}^2/\mathrm{s}^2$
$\mathbf{v}$, $\mathbf{v}_r$	= inertial and wind-relative velocity vectors, km/s
v, v_r	= magnitude of inertial and wind-relative velocities, km/s
W	= specific work, $\mathrm{km}^2/\mathrm{s}^2$
w	= kernel, $\mathrm{km}^2/\mathrm{s}^3$
x	= generalized distance
$\mathbf{y}$	= measurement vector, $\mathrm{km}^2/\mathrm{s}^2$
y	= net derived measurement, $\mathrm{km}^2/\mathrm{s}^2$
β	= drag ballistic coefficient, $\mathrm{km}^2/\mathrm{kg}$
$\Delta\tau$	= time spent by satellite in a cell, s
ϵ	= error
η_β	= ratio of reference to true β
θ	= inertial latitude, rad
λ	= smoothness constraint
μ	= Earth gravitational parameter, $\mathrm{km}^3/\mathrm{s}^2$
ξ	= two-body specific mechanical energy, $\mathrm{km}^2/\mathrm{s}^2$
ρ	= density, $\mathrm{kg}/\mathrm{km}^3$
ρ_0	= scale height density, $\mathrm{kg}/\mathrm{km}^3$
ϕ	= inertial longitude, rad

Subscript

1	= pass 1 stop time
2	= pass 2 stop time
d	= drag acceleration
in	= time inside the grid
meas	= measurement error
mod	= modeled density
model	= measurement model
ng	= non-gravitational acceleration
out	= time outside the grid
per	= change per period
pg	= perturbing gravity
srp	= solar radiation pressure
true	= true density, true measurement

Superscript

*	= reference
$\tilde{}$	= measured

I. Introduction

Inaccurate atmospheric drag models are the largest remaining error source affecting orbit prediction accuracy for most low-Earth orbit (LEO) satellites. The drag acceleration is typically modeled with

$$\mathbf{a}_{\mathrm{d}} = -\frac{1}{2}\beta\rho v_r \mathbf{v}_r \ , \tag{1}$$

where $\beta \equiv C_\mathrm{d}A/m$ is the ballistic coefficient containing the satellite's drag coefficient (C_d), drag cross-sectional area (A), and mass (m); $v_r = |\mathbf{v}_r|$ is the magnitude of the wind-relative velocity vector; and ρ is the density. Error in the modeled atmospheric density is a major contributing factor to errors in $\mathbf{a}_\mathrm{d}$. Several authors (e.g. [1–3]) have noted that little progress had been made in reducing the errors in modeled density from the 1960s until recently, during which time errors of 15% or more were common. Drag model errors of this magnitude can result in predicted satellite position errors on the order of 1 km or more after a single day [2, 4]. There has thus been much research attention in recent years on further improving density modeling for drag estimation.

Satellites have been used to study the upper atmosphere since the early days of space launches. References [2, 3, 5] contain some examples of historical overviews and recent advances in density modeling using satellite measurements. Broadly speaking, methods of estimating atmospheric density can be divided into those that use the motion of the satellite in the atmosphere, and those that use remote sensing methods (e.g. onboard spectroscopic sensing of upper atmospheric airglow [6]). The methods based on satellite motion can be further categorized into two groups: (1) those using tracking measurements, usually ground-based, of a large number of satellites, (2) and those using specialized onboard measurements, such as high-accuracy accelerometers and GPS receivers, on a small number of satellites.

Satellites with specialized onboard instruments have provided much useful data on density modeling. For example, the CHAMP and GRACE satellites are equipped with accelerometers and high-precision orbit estimation systems (e.g. GPS), which allow nearly continuous measurements of drag accelerations[7–10]. Because other factors that affect drag (mass, area, drag coefficient) are fairly well known for these satellites, the local density can be accurately estimated along the orbit. For example, McLaughlin et al.[4] demonstrated a sequential estimation scheme to estimate simultaneously the density and ballistic coefficient using high precision orbit ephemerides from the CHAMP satellite. A disadvantage of these approaches is that they are limited to a small number of specialized missions, making it difficult to apply the results to a global density model correction.

The other category of density estimation using tracking measurements is often used for atmospheric model calibration, where measurement data are typically more sparse in time and less accurate than those obtained using the onboard instruments described above. Examples in the literature can be loosely grouped into those using the actual ground-based tracking measurements, or those using publicly available data products, such as two-line element sets (TLEs) derived from those tracking measurements. Central to this discussion is the issue of the target satellite shape and attitude, since these parameters affect β, which can corrupt the density estimates.

TLEs are a well-known and often-studied source of orbit data for resident space objects. Picone et al. [11] developed a procedure for extracting the integrated density along a satellite's orbit using the mean motion contained in TLEs. Emmert et al. [12] used this method with TLEs from 5000 space objects to reconstruct a globally-averaged density value over a 40-year time span.

Nazarenko et al. [13] determined that the errors in estimated ballistic coefficients (i.e. obtained via an orbit estimation system) relative to their modeled values can be attributed to relative errors in the modeled density. These density model errors were parameterized using a polynomial function of altitude, and the polynomial coefficients were solved using a least-squares method, where the deviations in estimated and modeled ballistic coefficients from a set of satellites served as the measurements[14, 15]. Cefola et al. applied the method to TLEs as well[16].

The U.S. Air Force uses tracking measurements to estimate directly a correction to the Jacchia-70 (J70) empirical density model, in support of its High Accuracy Satellite Drag Model (HASDM)[17–21]. Corrections to the exospheric and inflection point temperatures in the vertical temperature profile are represented as two separate spherical harmonic expansions; the degree and order of these expansions vary in the literature, e.g. 2×2 in [17] and $4{\times}0$ in [18]. Sutton et al. [19] improved on this method by using a different set of basis functions to compute the temperature corrections. The number of tracked objects used by HASDM varies in the literature as well, but has ranged from around 70 satellites [17] up to 144 satellites [18]. Accurate estimates of the ballistic coefficients for the target calibration satellites are required[20]. These target satellites are tracked multiple times per orbital revolution[17] by the Space Surveillance Network (SSN) of radar and optical sensors[22], and a weighted least squares differential correction method is used across all targets that simultaneously solves for the density corrections and a state vector for each target [21]. The final estimated density corrections, in the form of 3-hourly fits to the data, are claimed to be within a few percent of the true density[21].

Both the HASDM approach and the work of Nazarenko, Cefola, et al. [14] are often called a Dynamic Calibration of the Atmosphere (DCA), because the methods are designed to provide time-varying density corrections. Vallado [23], pp. 569-570, gives additional overview and references related to DCA methods.

The contribution of the present paper is the description of a new DCA method, inspired by computed tomography (CT) methods, to correct atmospheric density models. Tomography is an inverse problem, with various applications in science and engineering, involving the inference of the properties of the material within a body using only measurements taken external to the body [24]. A good example is X-ray CT widely used in medical imaging (Figure 1). Here, X-rays with known intensities are emitted at various angles through a patient's body, where the final intensities of the rays are measured at a detector on the opposite side of the body. Let $f(x)$ be the X-ray attenuation coefficient of the tissue at point x, then an X-ray traveling a distance Δx will have a relative intensity loss of [25]

$$\frac{\Delta I}{I} = f(x)\Delta x \; . \tag{2}$$

Integrating over the path of the ray yields

$$\int \frac{dI}{I} = \int f(x)dx \; , \tag{3}$$

and given the known initial intensity I_0 and measured final intensity I_1 of the ray, the above integral becomes

$$\ln\left(I_1/I_0\right) = \int f(x)dx \; . \tag{4}$$

The inverse problem then involves: (1) discretizing the volume into cells, (2) rewriting the integral in Eq. (4) as a summation, (3) collecting the cell quantities and measurement for each ray into a linear equation, and (4) solving for the discretized $f(x)$ by inversion of the resulting system of linear equations. Since $f(x)$ is related to the density of the tissue, one can then construct a map of the internal density. Note also that because the matrix normal equation in the linear system derived from Eq. (4) is often ill-posed, it is common to use regularization to stabilize the system.

The approach in this paper is motivated by the analogy between the path of an X-ray beam through a solid object and the orbital path of a satellite through the upper atmosphere. In the case of the X-ray beam, the log of the attenuation factor is simply the integral of the attenuation coefficient along the path. At a more abstract level, a measurable quantity can be expressed as a path integral over the spatially varying quantity to be estimated. Since the state of a satellite along its orbit is continuously changing as a result of drag, which depends on the atmospheric density, a relationship is found between measurable orbital parameters (i.e. decay in specific mechanical energy) and density that can be written in the form of a path integral over the density, allowing tomographic reconstruction methods to be applied. No examples were found in the literature of this sort of tomography approach being applied to satellite orbital motion to deduce atmospheric density. Several studies have used satellite-based measurements with tomography and regularization (e.g. [26–30]), but usually the measurements involve radiometric observables from specialized onboard instruments (e.g. infrared, microwave), rather than the satellite orbital states themselves.

Others have used the decay in specific mechanical energy to study atmospheric density. Storz[31] used the measured energy dissipation extracted from the estimated ephemerides of a number of satellites, but the final estimated states in that study were similar to those used in HASDM (i.e. the spherical harmonic coefficients of the nighttime minimum exospheric temperature in the J70 model). This method was also used to validate the results of HASDM[32]. However, the estimator in [31, 32] used a least-squares differential corrector, in contrast with the regularization approach used here.

There are several advantages to the tomography approach described in this paper: 1) temporally sparse tracking data is assumed, in contrast to the HASDM method described above where the target satellites are tracked every revolution, 2) the method does not depend on a specific density model

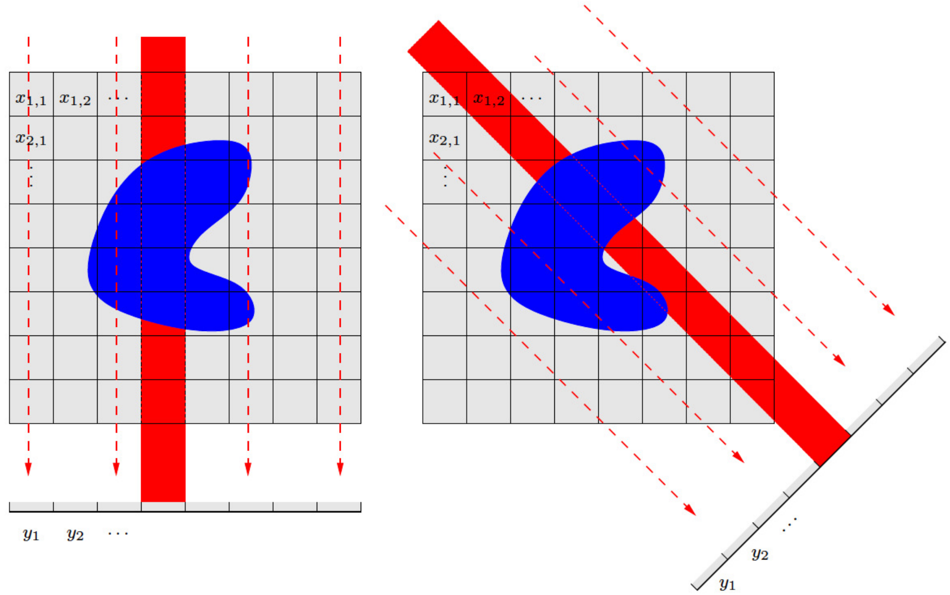

Fig. 1 Illustration of standard computed tomography: the region (gray box) containing an object of interest (blue shape) is discretized into many cells, and a known beam source (e.g. X-ray) is emitted towards a sensor at various angles. The red bars indicate the relationship between a sensor element and the cells (sometimes fractional) traversed by the part of the beam detected by that sensor. This relationship determines the linear equations that connect the cell densities with the measured values for each arrangement of the sensor with respect to the density grid.

parameterization, and hence it is straightforward to substitute any number of density models for which a scale factor is to be estimated, 3) Jacobians for the system dynamics or measurement model (e.g. describing the sensitivity of the dynamics with respect to the density states) are not needed, in contrast with typical differential corrector methods.

II. Tomography Applied to Satellite Orbits

This section describes how the tomography method is applied to a set of satellite tracking measurements. First, a grid is defined within a certain range of radial (r), inertial latitude (θ), and inertial longitude (ϕ) values. For simplicity, the latitude and longitude coordinates are defined in the inertial (J2000) reference frame, since the satellite positions will also be described in this frame. Thus, the grid will be nearly fixed relative to the Sun.*

The assumed set of target satellites have trajectories passing through the grid, either partially (e.g. an eccentric orbit with perigee falling within the grid) or in full (e.g. a nearly-circular LEO orbit). Each satellite is assumed to be visible to a ground-based tracking sensor for a minimum time span of a few minutes. During this "pass", the satellite is tracked by the sensor and measurements such as range, range rate, and angles are recorded. Although the details of the given sensor and orbit estimation scheme are unimportant for the current discussion, a sequential estimator is assumed, such that the measurements are processed and a final orbit estimate (OE) is generated at the pass stop time. For example, a typical OE would consist of the J2000 position and velocity vectors, and other solve-for parameters such as the satellite's ballistic coefficient β. The OE at the end of the first pass is then propagated to the start time of the next pass, where it is used as the initial

---

* The direction to the Sun will have a drift of approximately 1 degree per day in the inertial longitude direction using this grid definition.

state estimate for the second pass. The sequential estimation process then continues, processing the measurements during pass 2, and producing a new state estimate at the second pass stop time. This estimation process is then applied to each of the target satellites of interest.

Figure 2 illustrates this concept for several hypothetical LEO satellites (discussed in Section V), where the vertical axis shows the simulated specific mechanical energy, $\mathcal{E}$. For a given satellite, estimates of $(\mathbf{r}, \mathbf{v})$ are available at its t_1 (pass 1 stop time) and t_2 (pass 2 stop time). The specific mechanical energy $\mathcal{E}$ is then calculated from $(\mathbf{r}, \mathbf{v})$ at these times, and the change $\Delta\mathcal{E}$ over the time span from t_1 to t_2 is treated as the measurement input for the tomography. The final estimated density output from the tomography will effectively be the time-average of the temporal variations of the true density. The pass times do not need to occur simultaneously for all satellites, and depending on the number of sensors and their placement, these pass times may have some variation in time. Thus, in effect the tomography is estimating the time-average density between the mean pass 1 stop time and the mean pass 2 stop time.

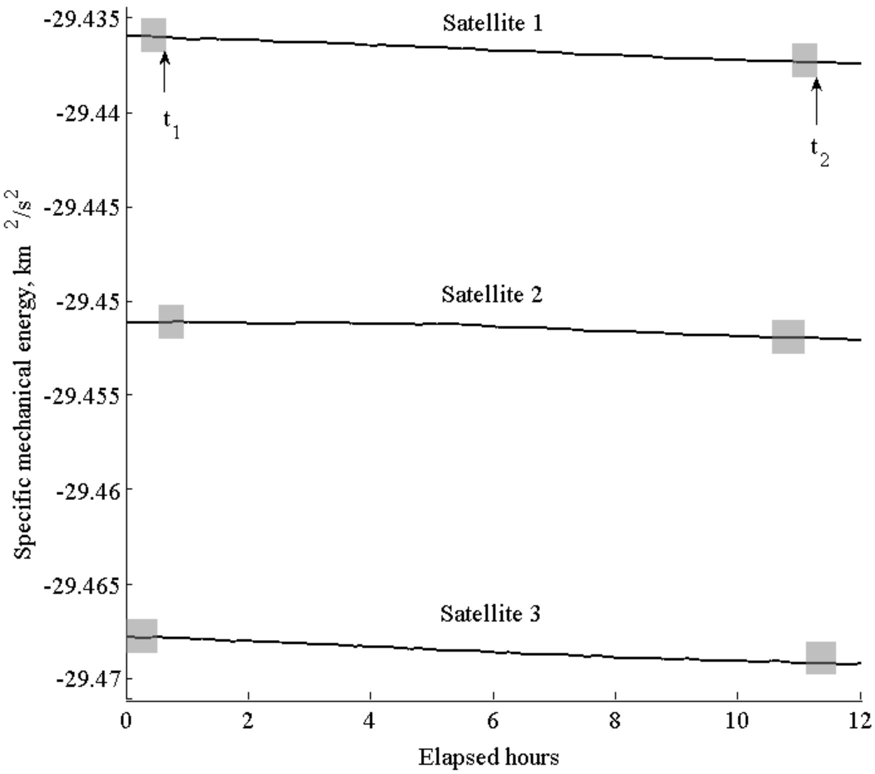

Fig. 2 Example of $\mathcal{E}$ for several LEO satellites, illustrating the orbit estimation scheme where each satellite has ground-station passes (denoted by gray boxes) occurring at potentially asynchronous times. Pass 1 stop time (t_1) and pass 2 stop time (t_2) are shown for the first satellite.

It is important to note that there are no constraints on the satellites' spatial position at t_1 and t_2, other than the visibility constraints of the chosen sensor geometry. For example, Satellite 1 could be observed at t_1 over the north pole, and several revolutions later it could be observed at t_2 near the equator, whereas Satellite 2 could be observed at both times at the same ground station at the south pole. However, it is assumed that there is a sufficient number of satellites with varying orbit orientation such that a global density field can be recovered.

III. Derivation of Measurement Equations

The measurement used in this tomography application is the specific work due to drag, which is related to the specific mechanical energy minus the specific work due to any other nonconservative forces. This section begins with two alternatives for reaching the desired equations: one is a direct method that uses work-energy principles, and the other is derived from Gauss's Variations of Parameters (VOP) for conservative and nonconservative perturbation forces. This section also gives approximate analytical equations for the measurements useful for designing the estimation system.

A. Specific mechanical energy and work

The change in specific mechanical energy $\mathcal{E}$ of a particle is equal to the sum of the changes in specific kinetic energy T and specific gravitational potential energy U, which in turn is equal to the specific net work done by the non-gravitational acceleration $\mathbf{a}_{\mathrm{ng}}$:

$$\Delta\mathcal{E} = \Delta T + \Delta U = \int\limits_{\mathcal{C}} \mathbf{a}_{\mathrm{ng}} \cdot d\mathbf{r} \ , \tag{5}$$

where the particle follows the trajectory $\mathcal{C} \in \mathbb{R}^3$ from t_1 to t_2. The gravitational potential energy represents that due to the Earth, including higher-order nonspherical effects, as well as that due to other bodies (e.g. lunisolar third-body effects). Let $\mathbf{a}_{\mathrm{ng}}$ be separated into the component due to drag, $\mathbf{a}_{\mathrm{d}}$, and the component due to all other nonconservative forces. For the level of fidelity required for the current problem, the only other nonconservative force considered is solar radiation pressure (SRP):

$$\Delta T + \Delta U - \int\limits_{\mathcal{C}} \mathbf{a}_{\mathrm{srp}} \cdot d\mathbf{r} = \int\limits_{\mathcal{C}} \mathbf{a}_{\mathrm{d}} \cdot d\mathbf{r} \ . \tag{6}$$

Recognizing that the specific work due to SRP is

$$W_{\mathrm{srp}} = \int\limits_{\mathcal{C}} \mathbf{a}_{\mathrm{srp}} \cdot d\mathbf{r}, \tag{7}$$

then Eq. 6 becomes

$$\Delta T + \Delta U - W_{\mathrm{srp}} = \int\limits_{\mathcal{C}} \mathbf{a}_{\mathrm{d}} \cdot d\mathbf{r} \ . \tag{8}$$

One may only be concerned with estimating the density up to a certain altitude, but a satellite on a high-eccentricity orbit may be passing through higher attitudes that still impart enough drag to perturb the orbit. Thus, for such cases it is necessary to separate the trajectory into portions "inside" and "outside" the grid in which the density correction factor will be estimated, hence:

$$\int\limits_{\mathcal{C}} \mathbf{a}_{\mathrm{d}} \cdot d\mathbf{r} = \int\limits_{\mathcal{C}_{\mathrm{out}}} \mathbf{a}_{\mathrm{d}} \cdot d\mathbf{r} + \int\limits_{\mathcal{C}_{\mathrm{in}}} \mathbf{a}_{\mathrm{d}} \cdot d\mathbf{r} \ . \tag{9}$$

The specific work due to drag outside the grid is

$$W_{\mathrm{d_{out}}} = \int\limits_{\mathcal{C}_{\mathrm{out}}} \mathbf{a}_{\mathrm{d}} \cdot d\mathbf{r} \ , \tag{10}$$

and Eq. 8 becomes

$$\Delta T + \Delta U - W_{\rm srp} - W_{\rm d_{out}} = \int\limits_{\mathcal{C}_{\rm in}} \mathbf{a}_{\rm d} \cdot d\mathbf{r} \ . \tag{11}$$

The modeled atmospheric density is related to the true atmospheric density via the unitless correction factor

$$s \equiv \rho_{\rm true}/\rho_{\rm mod} \ , \tag{12}$$

and thus Eq. 1 is rewritten as

$$\mathbf{a}_{\rm d} = -\frac{1}{2}\beta s \rho_{\rm mod} v_r \mathbf{v}_r \ , \tag{13}$$

The scale factor s is implicitly a function of $\mathbf{r}$ from its definition in Eq. 12. The right-hand side of Eq. 11, i.e. the specific work due to drag inside the grid, can be rewritten as

$$\int\limits_{\mathcal{C}_{\rm in}} \mathbf{a}_{\rm d} \cdot d\mathbf{r} = \int\limits_{t_{\rm in}} \mathbf{a}_{\rm d} \cdot \mathbf{v} dt \tag{14}$$

Define w, which has units of specific power, as

$$w \equiv \frac{\mathbf{a}_{\rm d} \cdot \mathbf{v}}{s} = -\frac{1}{2}\beta \rho_{\rm mod} v_r \mathbf{v}_r \cdot \mathbf{v} \ , \tag{15}$$

which makes Eq. 11 take the form

$$\Delta T + \Delta U - W_{\rm srp} - W_{\rm d_{out}} = \int\limits_{t_{\rm in}} wsdt \ . \tag{16}$$

The left-hand side of Eq. 16 can then be grouped into a net derived measurement y:

$$y = \int_{t_{\rm in}} wsdt \ . \tag{17}$$

It is now important to distinguish between the quantities that are measured, assumed known, and to be estimated. As described in Section II, the states $(\mathbf{r}, \mathbf{v})$ at t_1 and t_2 come from the assumed OE scheme, and from these, the measured changes in kinetic and gravitational potential energy, ΔT and ΔU, can be calculated. The density scale factor s is the quantity to be estimated via tomography. However, the terms $W_{\rm srp}$, $W_{\rm d_{out}}$, and w are implicitly dependent on $\mathbf{r}(t)$ and $\mathbf{v}(t)$ over the time span from t_1 to t_2, which are unknown. Using the OE output $(\mathbf{r}_1, \mathbf{v}_1)$ as the initial conditions, and assuming force model parameters, one can numerically integrate the equations of motion to give reference values of the position and velocity, denoted as $\mathbf{r}^*$ and $\mathbf{v}^*$. This process is described in more detail in Section V. After $(\mathbf{r}^*, \mathbf{v}^*)$ are calculated, the terms $W_{\rm srp}$ and $W_{\rm d_{out}}$ can be calculated using numerical integration (e.g. a trapezoidal method). The term $W_{\rm d_{out}}$ is evaluated using Eq. 13 with s set to unity, i.e. the density scale factor is not estimated outside the grid. Furthermore, β in Eq. 15 is not known perfectly, and thus must be assumed as the reference value β^*. The reference value β^* may be available from the OE scheme as a solve-for parameter, or it may be available via modeling[33, 34]. The value of β^* should be chosen carefully to avoid additional bias (e.g. as a result of inaccurate density models being used in the OE scheme). HASDM has a similar requirement on accurate ballistic coefficients; estimated values of β from a differential corrector for each satellite are averaged over many years, and comparisons made with calibrated spherical targets, to obtain values of β with reported accuracies of a few percent[20].

With this distinction in mind, Eq. 17 has the form of a Fredholm integral of the first kind, where w is the kernel representing the physical relationship between the unknown model s and observed data y [35]. Appendix A discusses in more detail the errors caused by assuming a reference trajectory and force model parameters in the measurement model.

B. Gauss's Variations of Parameters

The derivation from Gauss's VOP is as follows: using the Poisson brackets to derive the osculating orbit element rates from Lagrange's planetary equations [36], the variational equation for the semimajor axis a is

$$\frac{da}{dt} = \frac{\partial a}{\partial \mathbf{v}} \cdot \mathbf{a} \,, \tag{18}$$

where

$$\frac{\partial a}{\partial \mathbf{v}} = \frac{2a^2}{\mu}\mathbf{v} \,, \tag{19}$$

and $\mathbf{a}$ is the perturbing acceleration besides two-body gravitation. Therefore, combining Eqs. (18) and (19) and integrating both sides gives

$$\int_{a(t_1)}^{a(t_2)} \frac{da}{a^2} = \frac{2}{\mu} \int_{t_1}^{t_2} \mathbf{a} \cdot \mathbf{v} dt \,, \tag{20}$$

which can be rearranged as

$$\frac{1}{a(t_2)} - \frac{1}{a(t_1)} = -\frac{2}{\mu} \int_{t_1}^{t_2} \mathbf{a} \cdot \mathbf{v} dt \,. \tag{21}$$

Recalling that the two-body specific mechanical energy is $\xi = -\mu/(2a)$, multiply both sides of Eq. 21 by $-\mu/2$ to yield

$$\Delta\xi = \int \mathbf{a} \cdot \mathbf{v} dt \ . \tag{22}$$

Now, write the perturbing acceleration as

$$\mathbf{a} = \mathbf{a}_{\text{pg}} + \mathbf{a}_{\text{srp}} + \mathbf{a}_{\text{d}} \ , \tag{23}$$

where $\mathbf{a}_{\text{pg}}$ denotes the acceleration due to perturbing gravity for sources other than two-body. Thus, rewrite Eq. 22 as

$$\Delta\xi - \int\limits_{\mathcal{C}} \mathbf{a}_{\text{pg}} \cdot d\mathbf{r} - \int\limits_{\mathcal{C}} \mathbf{a}_{\text{srp}} \cdot d\mathbf{r} = \int\limits_{\mathcal{C}} \mathbf{a}_{\text{d}} \cdot d\mathbf{r} \ . \tag{24}$$

Noting that the specific work done by $\mathbf{a}_{\text{pg}}$ on the satellite is

$$\int\limits_{\mathcal{C}} \mathbf{a}_{\text{pg}} \cdot d\mathbf{r} = -\Delta U_{\text{pg}} \ , \tag{25}$$

where U_{pg} is the non-two-body gravitational potential energy, and recalling Eq. 7, then Eq. 24 becomes

$$\Delta\xi + \Delta U_{\text{pg}} - W_{\text{srp}} = \int\limits_{\mathcal{C}} \mathbf{a}_{\text{d}} \cdot d\mathbf{r} \ . \tag{26}$$

Because

$$\Delta\xi = \frac{v_2^2}{2} - \frac{\mu}{r_2} - \frac{v_1^2}{2} + \frac{\mu}{r_1} = \Delta T - \frac{\mu}{r_2} + \frac{\mu}{r_1} \ , \tag{27}$$

then Eq. 26 can be rewritten as

$$\Delta T - \frac{\mu}{r_2} + \frac{\mu}{r_1} + \Delta U_{\mathrm{pg}} - W_{\mathrm{srp}} = \int\limits_{\mathcal{C}} \mathbf{a}_{\mathrm{d}} \cdot d\mathbf{r} \; . \tag{28}$$

Now, let U denote the combined gravitational potential energy, i.e. that due to two-body and perturbing gravity, allowing Eq. 28 to become

$$\Delta T + \Delta U - W_{\mathrm{srp}} = \int\limits_{\mathcal{C}} \mathbf{a}_{\mathrm{d}} \cdot d\mathbf{r} \; , \tag{29}$$

which is the same result as Eq. 8.

C. Approximate measurement

It is instructive to analyze the magnitude of the measured quantity y and its variation with satellite altitude and ballistic coefficient, because the specific work due to drag is not commonly encountered in practice. This analysis is simplified by treating the satellite's trajectory as either a circle or an ellipse, restricting the analysis to a single orbital period, and ignoring other forces besides drag and the two-body gravity.

To first examine the circular orbit case, let the drag acceleration from Eq. 1 act parallel to the velocity, and assume it is constant over the path of the orbit: $|\mathbf{a}| = \rho\beta v^2/2$ acting in the anti-velocity direction. Because the circular orbit velocity is $v = \sqrt{\mu/r}$, and over one period the satellite will travel a distance of $2\pi r$, then from Eq. 26, where U_{pg} and W_{srp} are assumed to be zero, the change in ξ over one period is

$$\Delta\xi_{\mathrm{per}} = -\pi\beta\mu\rho \; . \tag{30}$$

For this approximate analysis, an exponential model of the density is used:

$$\rho = \rho_0 \exp\left(\frac{R - r}{H}\right) , \tag{31}$$

where the values of $H = 59.06$ km and $\rho_0 = 3.875 \times 10^{-9}$ kg/m^3 are obtained by fitting a line to the density profile above 200 km altitude given in Fig. 2.2(a) of [37], resulting in

$$\Delta\xi_{\mathrm{per}} = -\pi\beta\mu\rho_0 \exp\left(\frac{R - r}{H}\right) . \tag{32}$$

Thus, under these assumptions, $\Delta\xi_{\mathrm{per}}$ varies linearly with β at a fixed r, and it varies exponentially with r at a fixed β. Figure 3 shows $\Delta\xi_{\mathrm{per}}$ for a circular orbit for a range of values. It can be seen that over the typical values of β and r of interest (i.e. for satellites in the thermosphere, with $\beta \sim 0.01$ m^2/kg being representative of some HASDM targets[20]), $\Delta\xi$ due to drag will be on the order of 10^{-4} km^2/s^2 per orbit.

To obtain the approximate change in energy over one orbital period for an ellipse, it is convenient to start with the following equation for the derivative of a with respect to the eccentric anomaly E from pp. 670 of [23], also derived using Gauss's VOP with drag:

$$\frac{da}{dE} = -\beta \frac{\rho a^2 (1 + e\cos E)^{3/2}}{\sqrt{1 - e\cos E}} \; . \tag{33}$$

Rearrange to obtain:

$$\frac{da}{a^2} = -\beta \frac{\rho (1 + e\cos E)^{3/2}}{\sqrt{1 - e\cos E}} dE \; , \tag{34}$$

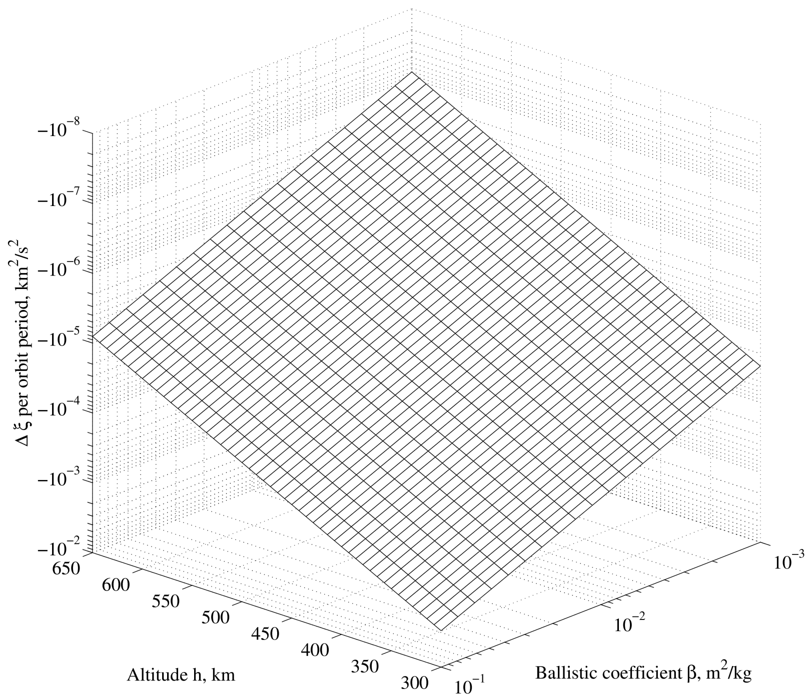

Fig. 3 Approximate change in ξ due to drag over one period for a circular orbit

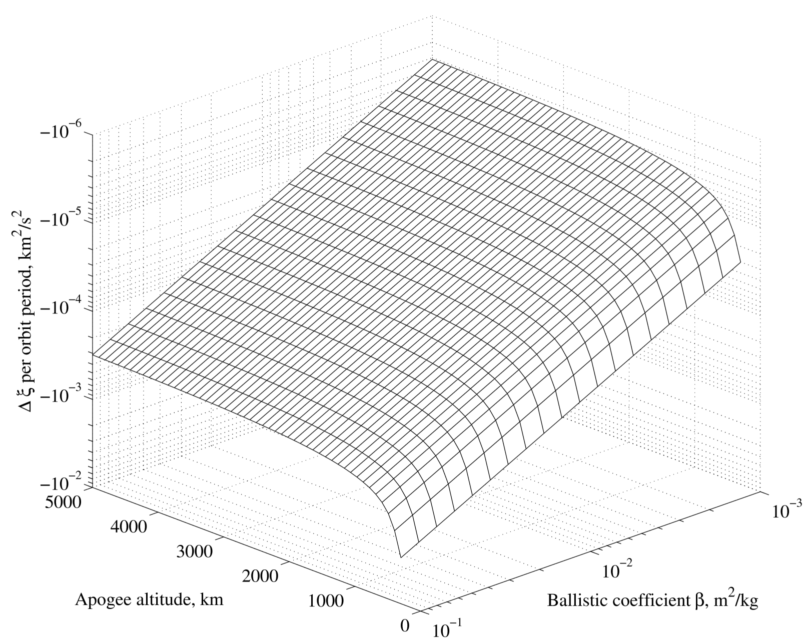

Fig. 4 Approximate change in ξ due to drag over one period for an elliptical orbit with fixed perigee altitude of 300 km, and varying apogee altitude and ballistic coefficient.

and similar to the development after Eq. 20, integrate both sides and multiple by $\mu/2$ to obtain

$$\Delta\xi_{\text{per}} = -\frac{\mu\beta}{2}\int_0^{2\pi} \frac{\rho(1+e\cos E)^{3/2}}{\sqrt{1-e\cos E}} dE\ . \tag{35}$$

Recall that here, the simple density model from Eq. 31 is used, and $r = a(1 - e\cos E)$. The integral on the right-hand side of Eq. 35 is evaluated numerically using an adaptive Simpson quadrature, resulting in the surface shown in Fig. 4. This figure shows that, keeping perigee altitude fixed at 300 km and increasing apogee altitude, the corresponding change in energy per orbit will decrease in magnitude.

The surfaces in Figures 3 and 4 are compared in Section VI to numerical simulations for verification, and are useful for determining the approximate magnitude of the measurement signal when planning observations of actual satellite targets.

IV. Solving for Density Scale Factor

The linear system in Eq. 17 is solved by first discretizing the integral and then writing in matrix form. A spatial grid with cell indices $n \in \{1, \ldots, N\}$ is defined, where s_n is assumed uniform in each cell. For satellite $i \in \{1, \ldots, M\}$, the equations of motion are numerically propagated, with time step Δt, as described above, resulting in discrete values of $\mathbf{r}_k^*$ and $\mathbf{v}_k^*$. Here, $k \in \{K_{i,n}\}$ represents the time instances that satellite i is in cell n, and is a subset of this satellite's total propagated times. The integral in Eq. 17 is replaced by a summation by discretizing along the satellite's trajectory through the grid (Fig. 5)

$$y_i = \begin{bmatrix} w_{i,1}\Delta\tau_{i,1} & \cdots & w_{i,N}\Delta\tau_{i,N} \end{bmatrix} \begin{bmatrix} s_1 & \cdots & s_N \end{bmatrix}^T\ . \tag{36}$$

where $\Delta\tau_{i,n}$ is the time spent by satellite i in cell n, and $w_{i,n}$ is the averaged quantity $w(t, \mathbf{r}^*, \mathbf{v}^*)$ for satellite i in cell n, i.e.

$$w_{i,n} = \frac{1}{P_{i,n}} \sum_{k\in K_{i,n}} w(t_k, \mathbf{r}_k^*, \mathbf{v}_k^*)\ , \tag{37}$$

where $P_{i,n}$ is the number of times satellite i is in cell n.

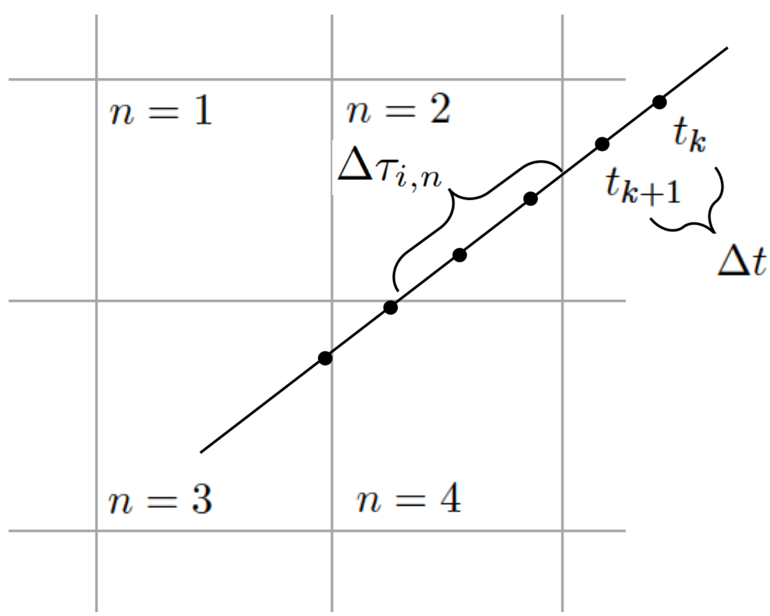

Fig. 5 Illustration of grid (gray) with satellite orbit (black) propagated at finite time t_k.

Using the approximation

$$\Delta\tau_{i,n} \approx P_{i,n}\Delta t \ , \tag{38}$$

then from Eq. 37:

$$w_{i,n}\Delta\tau_{i,n} \approx \Delta t \sum_{k\in K_{i,n}} w(t_k, \mathbf{r}_k^*, \mathbf{v}_k^*) \ . \tag{39}$$

For ease of notation, define

$$h_{i,n} \equiv \sum_{k\in K_{i,n}} w(t_k, \mathbf{r}_k^*, \mathbf{v}_k^*) \ , \tag{40}$$

then the matrix form of Eq. (36) that includes all satellites M is

$$\begin{bmatrix} y_1 \\ \vdots \\ y_M \end{bmatrix} = \Delta t \begin{bmatrix} h_{1,1} & \cdots & h_{1,N} \\ \vdots & \ddots & \vdots \\ h_{M,1} & \cdots & h_{M,N} \end{bmatrix} \begin{bmatrix} s_1 \\ \vdots \\ s_N \end{bmatrix} \ . \tag{41}$$

Note that in general a given satellite will not pass through each cell in the grid. If a satellite does not pass through a cell, then $h_{i,n} = 0$ for that cell.

Equation 41 can be written concisely as $\mathbf{y} = \mathcal{H}\mathbf{s}$, where

$$\mathcal{H} \equiv \Delta t \begin{bmatrix} h_{1,1} & \cdots & h_{1,N} \\ \vdots & \ddots & \vdots \\ h_{M,1} & \cdots & h_{M,N} \end{bmatrix} \ , \tag{42}$$

$$\mathbf{s} \equiv \begin{bmatrix} s_1 & \cdots & s_N \end{bmatrix}^T \ . \tag{43}$$

In general, this is an ill-posed problem because $N > M$ and the matrix $\mathcal{H}$ is sparse. This problem is solved using Tikhonov regularization [38]:

$$\underset{\mathbf{s}}{\operatorname{argmin}} \frac{1}{2}\|\mathcal{H}\mathbf{s} - \mathbf{y}\|_2^2 + \frac{\lambda}{2}\|D\mathbf{s}\|_2^2 \ , \tag{44}$$

the solution for which can be expressed in closed-form as

$$(\mathcal{H}^T\mathcal{H} + \lambda D^T D)\mathbf{s} = \mathcal{H}^T\mathbf{y} \ , \tag{45}$$

which can be solved using a variety of standard methods [39]. The simulations in the present study solve Eq. 45 using the conjugate gradient method, with a relative error tolerance of 10^{-7}. A discretization of the three-dimensional gradient $\nabla\mathbf{s}$ is chosen as the regularization operator D because $\mathbf{s}$ is expected to be a spatially smooth field. (Total variation regularization [40] is not chosen because discontinuities are not expected.) In Eq. 45, the operation $D^T D\mathbf{s}$ acting on the vector $\mathbf{s}$ is implemented in practice as a function that takes in a $N \times 1$ vector $\mathbf{s}$, reorders it into a three-dimensional matrix representing the chosen spatial coordinates, computes the gradients D and D^T using a finite difference, and returns the result as another $N \times 1$ vector.

Although reasonable results are obtained using the simple gradient in Cartesian coordinates, somewhat better results are obtained in this study by representing the present problem in spherical coordinates:

$$\nabla s = \left(\frac{\partial s}{\partial r}, \frac{1}{r}\frac{\partial s}{\partial\theta}, \frac{1}{r\sin(\theta)}\frac{\partial s}{\partial\phi}\right) \ . \tag{46}$$

For notational simplicity Eq. 44 is defined using a single regularization parameter λ, but for additional flexibility this problem can be expressed using individual terms for each component of the gradient, denoted as λ_r, λ_θ, and λ_ϕ:

$$\underset{\mathbf{s}}{\operatorname{argmin}} \frac{1}{2}\|\mathcal{H}\mathbf{s}-\mathbf{y}\|_2^2 + \frac{\lambda_r}{2}\|D_r\mathbf{s}\|_2^2 + \frac{\lambda_\theta}{2}\|D_\theta\mathbf{s}\|_2^2 + \frac{\lambda_\phi}{2}\|D_\phi\mathbf{s}\|_2^2 \ . \tag{47}$$

Hence, Eq. 45 becomes

$$(\mathcal{H}^T\mathcal{H} + \lambda_r D_r^T D_r + \lambda_\theta D_\theta^T D_\theta + \lambda_\phi D_\phi^T D_\phi)\mathbf{s} = \mathcal{H}^T\mathbf{y} \ . \tag{48}$$

The angular gradients D_θ and D_ϕ can be made unitless by replacing the numerator in the $1/r$ term in Eq. 46 with a reference radial distance, for example the lower grid boundary. Thus, the units of λ_θ and λ_ϕ are the same as y^2, i.e. km^4/s^4. The units of the gradient D_r are km^{-1}, and thus λ_r has units of km^6/s^4. The process of selecting suitable values of λ is discussed in Section VII.

V. Simulation Setup

This section describes numerical simulations used to test the tomography method. The grid is defined as follows: the radial direction boundaries are chosen as 6678 to 6878 km (300 to 500 km altitude), to capture a reasonable slice of the thermosphere, with 100 km uniform spacing; the inertial longitude direction is -180° to 180°, with 20° uniform spacing; and the inertial latitude direction is -90° to 90°, with 20° uniform spacing. The resulting number of grid cells is $N = 324$.

Figure 6 shows a flow chart of the tomography process, including the simulated satellite orbits used in this study. For a given simulation run, the initial ground-truth Cartesian states $\mathbf{r}(t_1)$ and $\mathbf{v}(t_1)$ are generated from a random sampling of $M = 50$ LEO satellite orbits as follows. First, the radius of perigee r_p and radius of apogee r_a are sampled from a uniform distribution between 6703 to 6853 km (325 to 475 km altitude). The initial a and e then follow from $a = (r_p + r_a)/2$ and $e = (r_a - r_p)/(r_a + r_p)$. The initial values of inclination, right-ascension of the ascending node, argument of perigee, and true anomaly are all sampled from a uniform distribution from 0 to 2π rad. These initial osculating Keplerian elements are then converted to $\mathbf{r}(t_1)$ and $\mathbf{v}(t_1)$. In this simulation, the actual ground sites for tracking are not specified, and instead the orbits are assumed to be estimated at t_1, and again 12 hours later at t_2. In addition to the 50 LEO satellites used to demonstrate the tomography method, 50 higher-eccentricity orbits are simulated in each run for comparison in Section VI and Appendix A.

As described in Section II, during actual operation of the system, a given satellite would be observed during two passes over one or more ground stations, after which two estimates of the orbital states would be generated (dashed box in Figure 6). These estimated states at t_1 and t_2 are denoted with $(\tilde{\mathbf{r}}_1, \tilde{\mathbf{v}}_1)$ and $(\tilde{\mathbf{r}}_2, \tilde{\mathbf{v}}_2)$, respectively†. For the current simulations, as shown in Fig. 6, each satellite is propagated twice. One propagation represents the ground-truth $(\mathbf{r}, \mathbf{v})$, where the force model parameters are known. The other propagation represents the assumed trajectory $(\mathbf{r}^*, \mathbf{v}^*)$. To simulate reasonable orbit estimation uncertainty for a typical ground-based sensor (e.g. optical telescope)[41], Gaussian noise is added to $(\mathbf{r}, \mathbf{v})$ to generate $(\tilde{\mathbf{r}}, \tilde{\mathbf{v}})$, with 1 m ($1\sigma$) position and 1 mm/s ($1\sigma$) velocity variance in each Cartesian component. Furthermore, to simulate imperfect knowledge of force model parameters, errors in β^* of 5% (1σ) are added during the propagation of $(\mathbf{r}^*, \mathbf{v}^*)$.

The numerical propagator is a special perturbations propagator using Cowell's formulation (pp. 523 of [23]) with the Cartesian position and velocity. A 4th order Runge-Kutta method with a step size of $\Delta t = 10$ s is used to integrate the equations of motion. For the Earth's nonuniform gravity, it uses a 7×7 spherical harmonic expansion with the EGM96 coefficients (pp. 987 of [23]). Also included are third-body effects from the Sun and Moon, and SRP accelerations (where these force model parameters are assumed known). The third-body forces use the DE405 planetary

† Although it is common in the literature to denote estimated quantities with a hat (̂), this study uses a tilde (̃) for measured quantities, to emphasize that the position and velocity serve as measured inputs into the tomography process, and also because the specifics of the orbit estimation system are not treated here in detail.

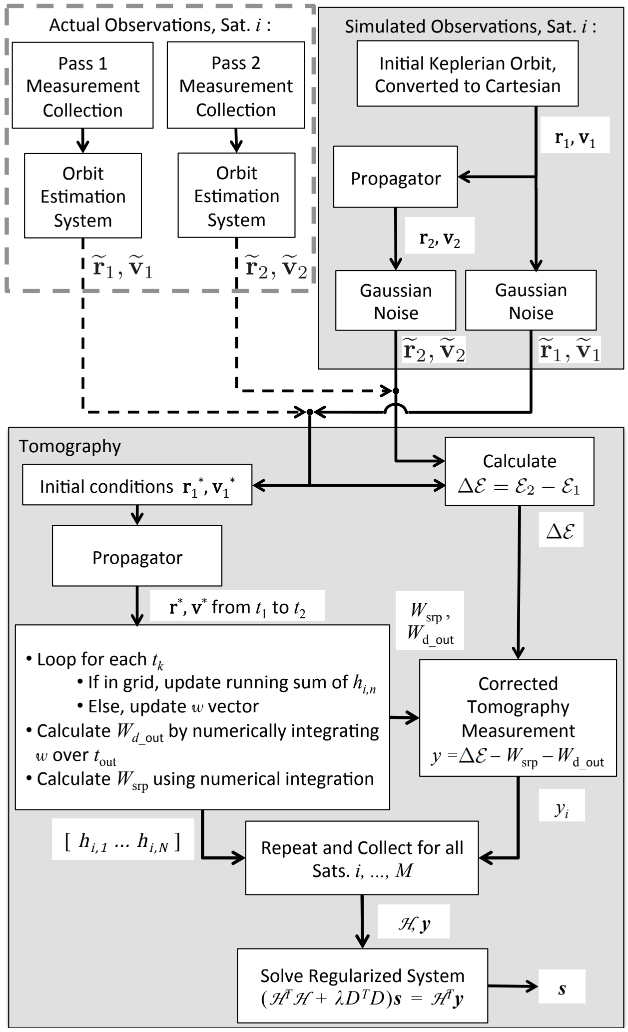

Fig. 6 Flow chart of tomography process, showing operation with both simulated measurements as used in the current study (gray box in upper right), and actual observations (dashed box in upper left).

ephemerides via JPL's SPICE toolkit[‡]. The SRP force calculation uses a simple cannonball model (i.e. one coefficient of reflectivity of 1.0 for each satellite), using the same area A as the atmospheric drag, and a cylindrical Earth eclipse model (pp. 577 of [23]). The Global Ionosphere-Thermosphere Model (GITM) [42] is used to represent the true density ρ_{true}, and the NRLMSISE-00 model [43] is used as the modeled density ρ_{mod}. A constant ballistic coefficient of 2.2×10^{-2} m^2/kg is used for the truth value of β for each satellite. The current simulation assumes no winds for the propagation of both the ground-truth $(\mathbf{r}, \mathbf{v})$ and the reference orbits $(\mathbf{r}^*, \mathbf{v}^*)$, and instead uses a simple co-rotating atmosphere model in the calculation of $\mathbf{v}_r$.

VI. Simulation Results

The simulation was run 10 times over the same time interval, resulting in a total of 1000 random satellite orbit propagations (i.e. 500 LEO orbits, and 500 higher-eccentricity orbits for comparison).

[‡] http://naif.jpl.nasa.gov/naif/toolkit.html, accessed October 1, 2012

A given run uses 50 LEO orbits to calculate the tomography solution.

The points in Fig. 7 show the absolute value of the actual work due to drag for each satellite, calculated using $y = \Delta\mathcal{E} - W_{\text{srp}} - W_{\text{d}_{\text{out}}}$. The horizontal axis shows the semilatus rectum $p = a(1-e^2)$ of each truth obit at t_1. Also shown in Figure 7 are curves generated using Eqs. 32 and 35 for the approximate measurement $\Delta\xi_{\text{per}}$ (again using the absolute value). The solid gray line shows the approximate measurement $\Delta\xi_{\text{per}}$ for a circular orbit, where the line has been scaled by a factor of 8 to account for the approximate number of periods experienced by a LEO satellite over 12 hours. The dashed and solid black curves represent the corresponding values from Eq. 35, assuming perigee at 300 and 500 km, respectively, scaled by 6 orbital periods. Note that the curves representing the approximate relations from Eqs. 32 and 35 use the simple exponential density model from Eq. 31, whereas the points use the NRLMSISE-00 modeled density. It is apparent from this figure that the approximate relations developed in Section III C are suitable approximations of the measurement signal y, especially for the LEO orbits. Also apparent is that the magnitude of y decreases as p increases.

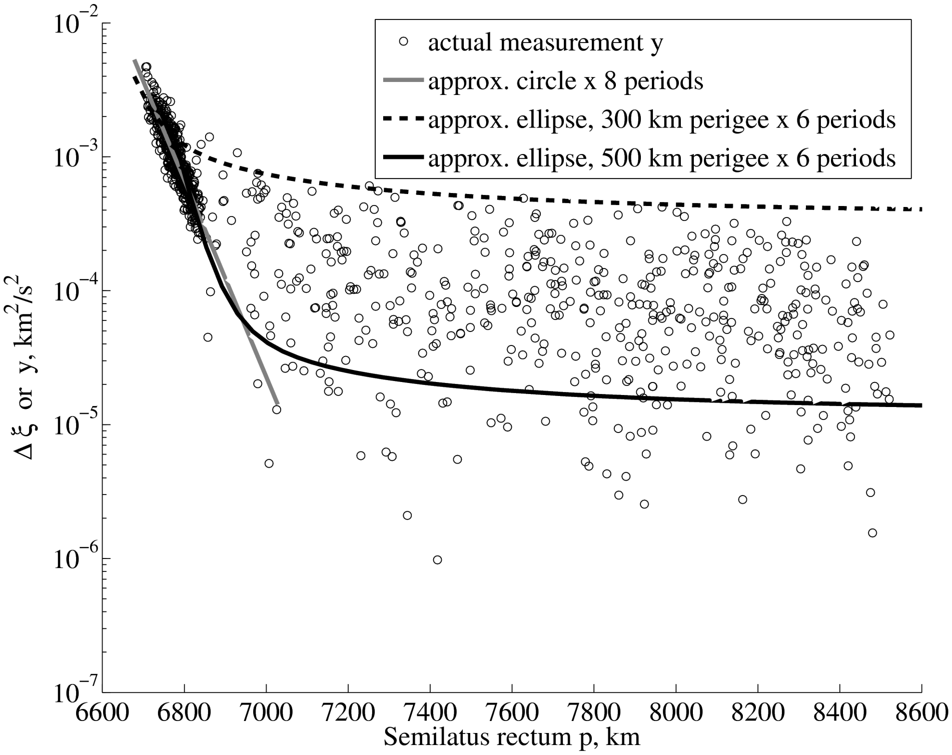

Fig. 7 Absolute value of measurement signal y for 1000 simulated orbits, and approximate values of $\Delta\xi$ per period.

Figure 8 shows the time-average of the true $s = \rho_{\text{true}}/\rho_{\text{mod}}$ value, evaluated over the same grid as defined above, where a slice is taken at 350 km altitude. Figure 9 shows the corresponding slice of the estimated s field, using the following regularization parameters: $\lambda_\theta = 1 \times 10^{-8}$ km^4/s^4, $\lambda_\phi = 1 \times 10^{-8}$ km^4/s^4, and $\lambda_r = 1 \times 10^{-2}$ km^6/s^4. It can be seen that overall there is good agreement between the two, e.g. the region of $s \approx 0.7$ is apparent in both figures centered around 0 deg latitude and -100 deg longitude. However, there are some finer structures apparent in Figure 8 that are not quite visible in Figure 9. Figures 10 and 11 show the corresponding results for the slice at 450 km altitude, and the overall results are similar.

Figures 12 and 13 show the percent error between the estimated **s** and the time-averaged ground truth, for each altitude slice, from simulation run 1. It is clear that the density correction in most cells are estimated to within 0 to 20%, with a few cells at 450 km altitude having higher error around 50%.

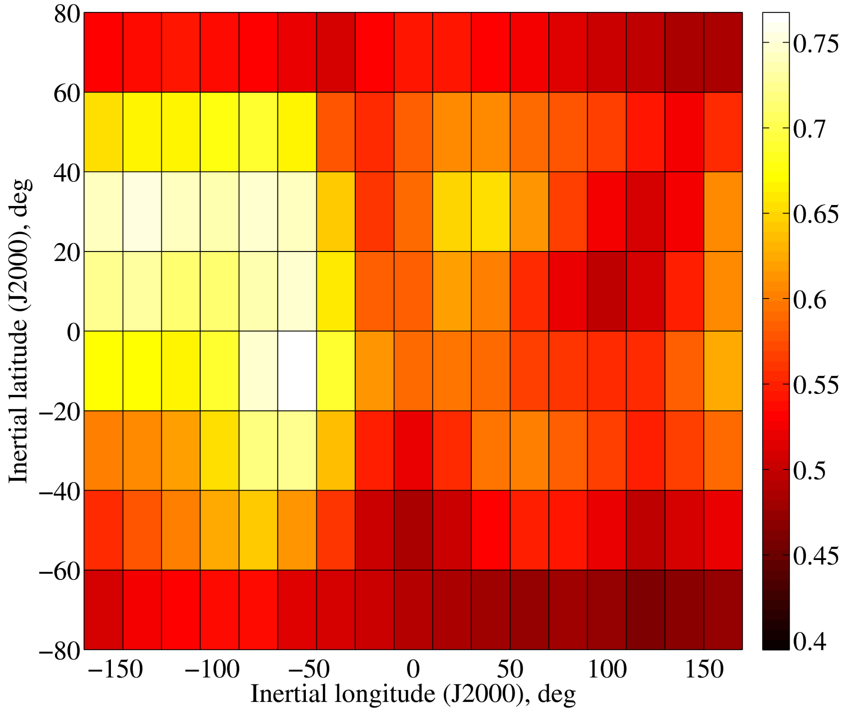

Fig. 8 True time-averaged $s = \rho_{\mathrm{true}}/\rho_{\mathrm{mod}}$, at 350 km alt.

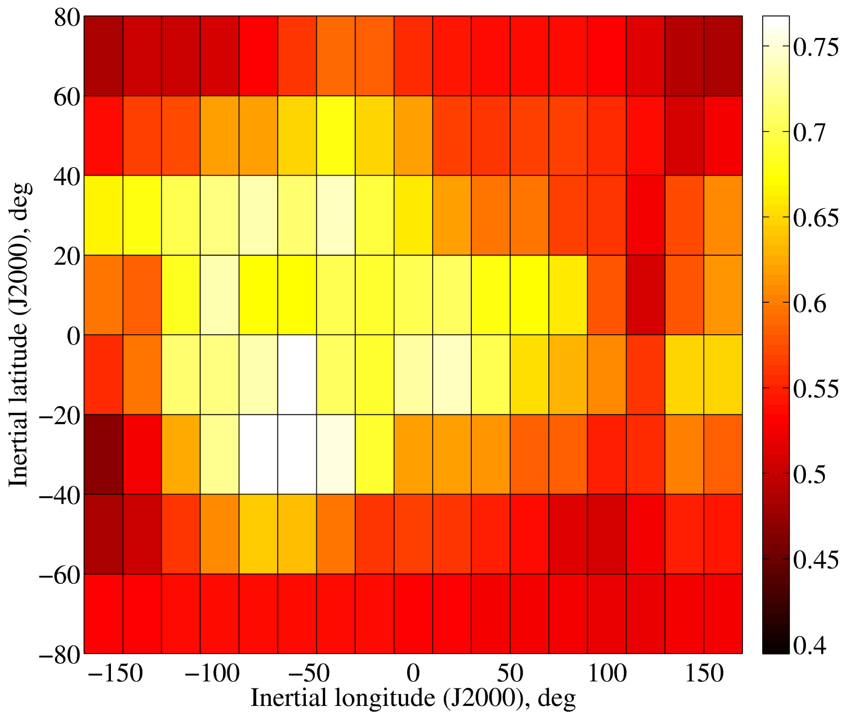

Fig. 9 Estimated time-averaged $s = \rho_{\mathrm{true}}/\rho_{\mathrm{mod}}$ for run 1, at 350 km alt.

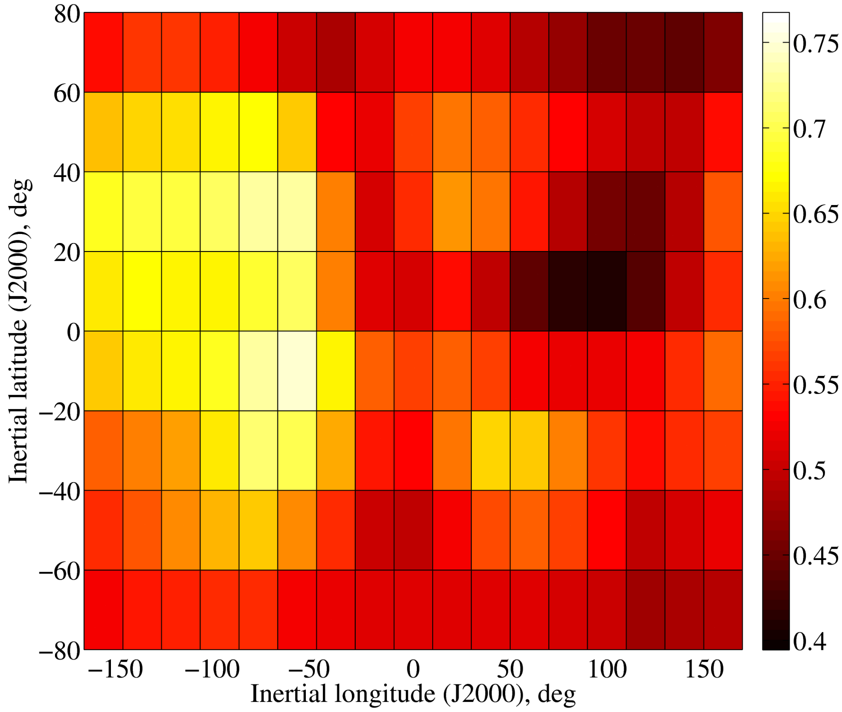

Fig. 10 True time-averaged $s = \rho_{\text{true}}/\rho_{\text{mod}}$, at 450 km alt.

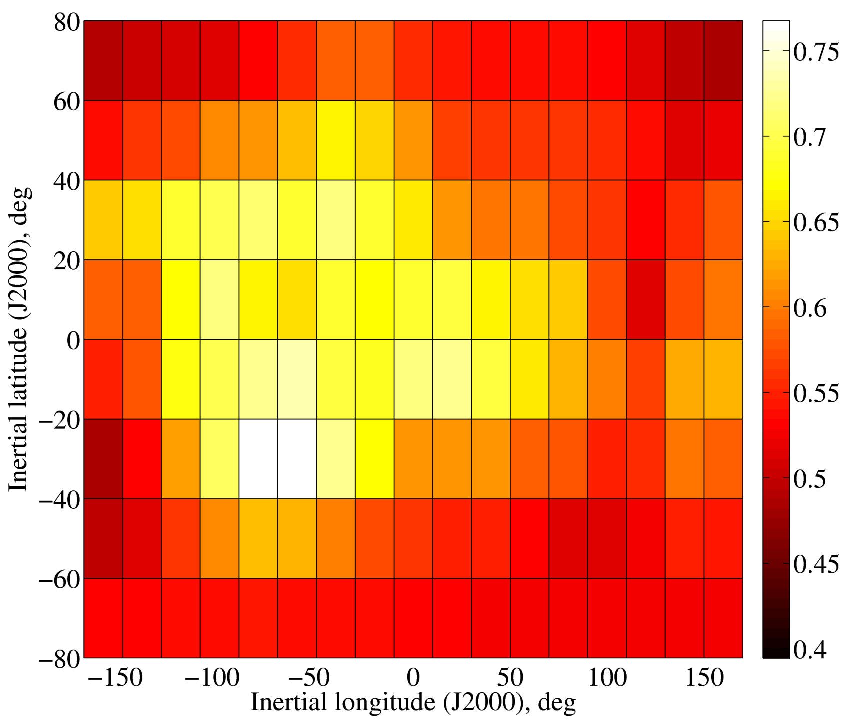

Fig. 11 Estimated time-averaged $s = \rho_{\text{true}}/\rho_{\text{mod}}$ for run 1, at 450 km alt.

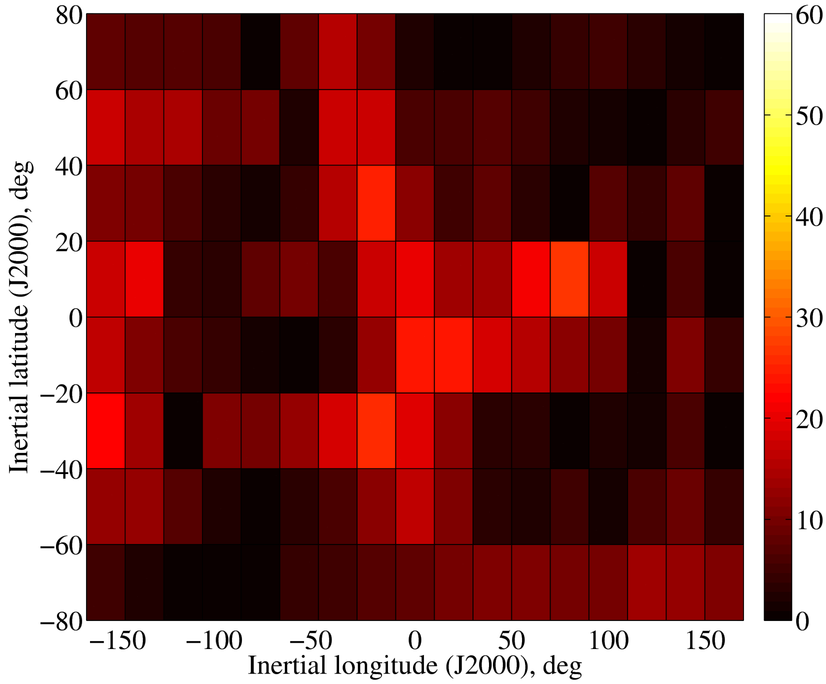

Fig. 12 Percent error in estimated s for run 1, at 350 km alt.

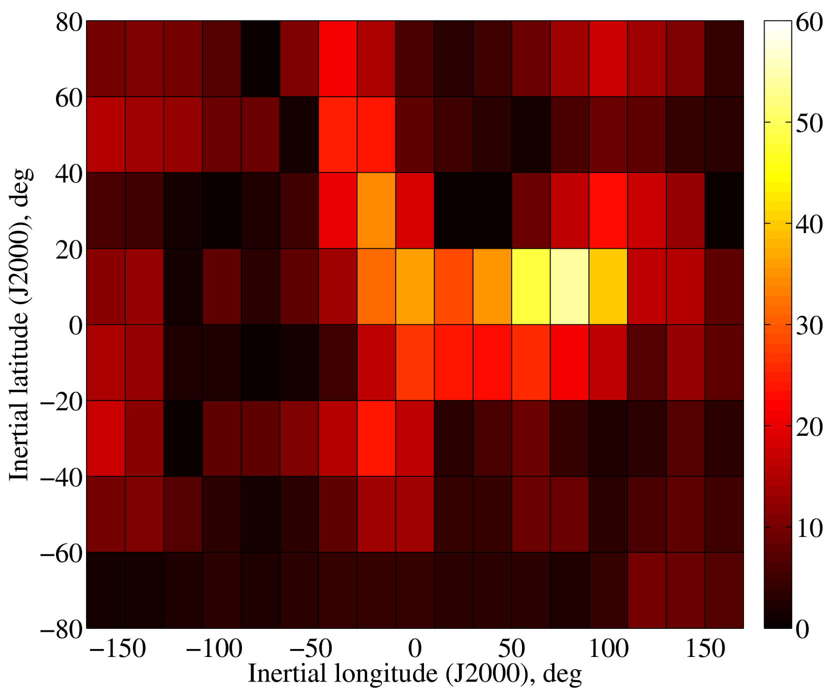

Fig. 13 Percent error in estimated s for run 1, at 450 km alt.

Figure 14 shows the root mean square (RMS) error, between the time-averaged ground-truth $\mathbf{s}$ and the estimated $\mathbf{s}$, for each altitude slice, and for the 10 different runs of the tomography simulation.

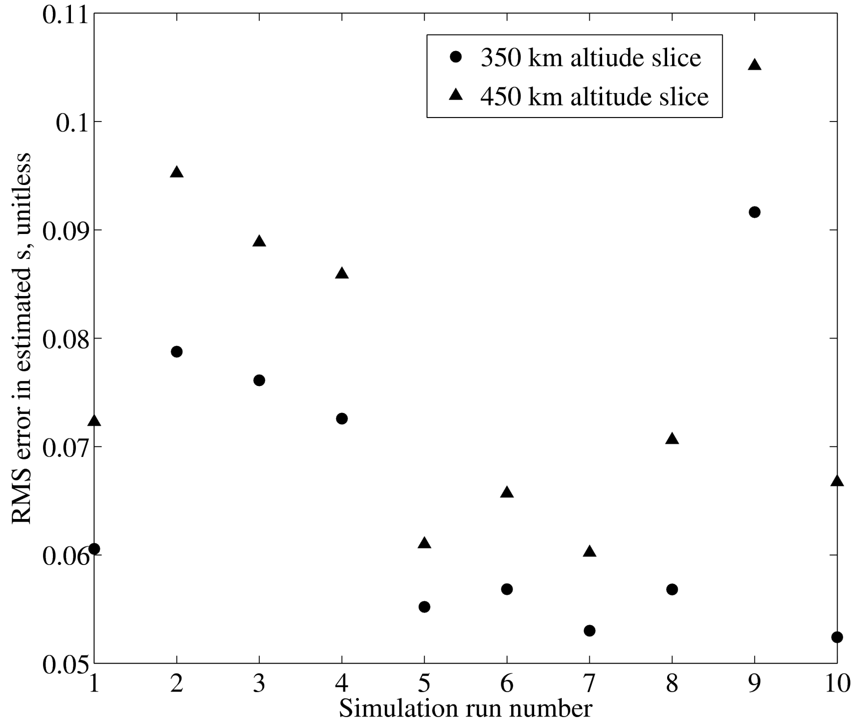

Fig. 14 RMS error in estimated s relative to time-averaged truth s, for 10 different simulation runs.

The results from Figures 9 through 13 correspond to the first run in Figure 14 (representing a fairly average result). It is evident that the tomography has similar performance when using different sets of orbits; the average RMS error in **s** is approximately 0.07 (unitless). Considering that the spatial average of the time-averaged truth **s** is around 0.65 (recall Figures 8 and 10), then the estimated **s** agrees to around 10%.

VII. Discussion

The true density will, in reality, have small variations in time relative to the time-averaged value, so there would be some additional errors if one were to compare the estimated time-average **s** with the instantaneous true density. For example, in the simulation scenario discussed above, the instantaneous density varied only by a few percent relative to the time-averaged value. However, additional simulations should be performed in future work to ensure that the tomography method described here would also be feasible in cases where the instantaneous density varies greatly about its time-averaged value, e.g. during increased solar activity.

One drawback of the method is that setting the numerical value of the smoothness constraints $(\lambda_r, \lambda_\theta, \lambda_\phi)$ requires some tuning to produce acceptable results in the final estimated **s** field. Figure 15 shows the RMS error in the estimated **s** with varying values for the smoothness constraints, which gives an indication of the sensitivity of the solution accuracy to the choice of λ. Larger values of λ produce more smoothed results, which is an expected result when using the Tikhonov regularization formulation (recall Eq. 44). In this study, it was found that a good initial guess for λ_θ and λ_ϕ was to use the square of the approximate measurement value $\Delta\xi$ from Figure 7 (this point is apparent when recalling the discussion on the units of λ in Section IV). In practice (i.e. when the ground-truth density is unknown), it is fairly straightforward to tune the values of λ_θ and λ_ϕ by viewing the resulting estimated **s** field: setting λ too large results in a uniform **s** field, and setting λ too small causes the $\mathbf{s}$ field to resemble random noise. This trend is apparent when recalling Figure 15, because using λ_θ and λ_ϕ larger than approximately 10^{-6} km^4/s^4 resulted in nearly uniform $\mathbf{s}$ (over-smoothing), and using values smaller than approximately 10^{-9} km^4/s^4 resulted in noisy $\mathbf{s}$ (under-smoothing). It was found that using a larger value for λ_r than that used in λ_θ and λ_ϕ produced good results. If λ_r was set too small, the higher altitude density slice was poorly estimated. Using a larger λ_r effectively constrains the higher altitude slice to more closely match the lower altitude slice, where the drag effects are more noticeable on the satellite orbits for a given time span. Likewise, Fig. 14 shows that the lower altitude slice was more accurately estimated than the higher altitude slice; for a constant measurement time span (12 hours in this case) independent of altitude, the drag effects at lower altitude produce a stronger measurement signal.

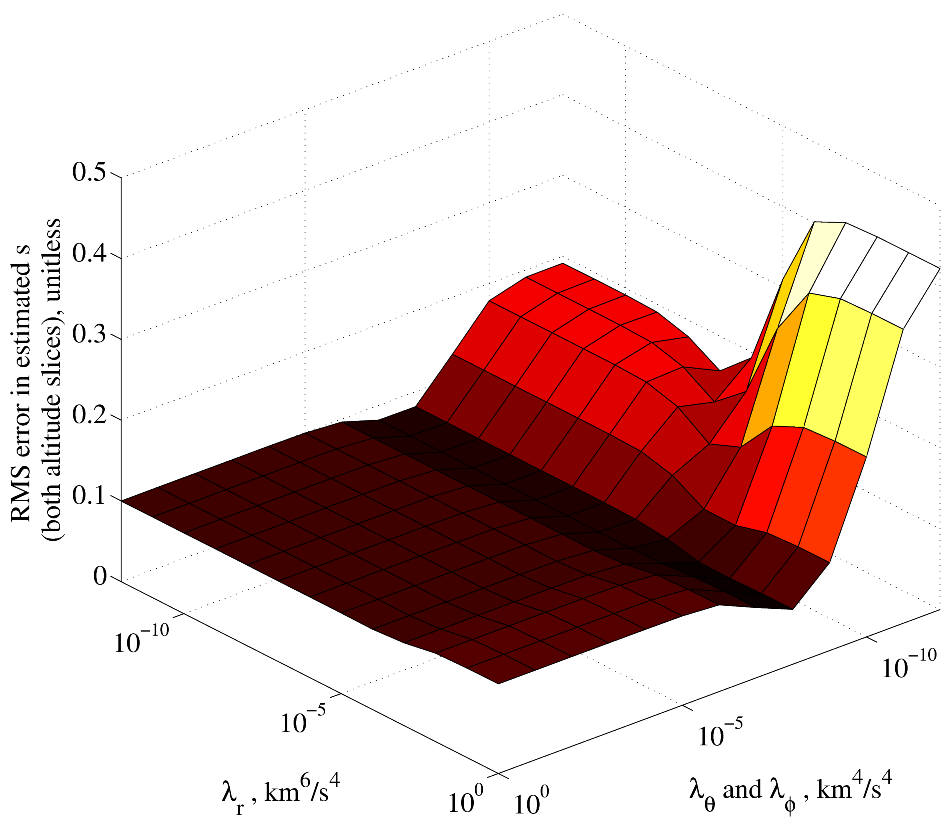

Fig. 15 RMS error in estimated s from run 1, with varying smoothness constraints λ_θ, λ_ϕ, and λ_r.

The error analysis (Appendix A) does not address errors introduced by the approximation in Eq. 38 or the discretization of the trajectory across the grid. The suitability of the averaged quantity $w_{i,n}$ (Eq. 37) depends on the number of points $P_{i,n}$, which in turn depends on the integration time step Δt, size of each cell, and number of orbital revolutions. Thus, these parameters can be tuned as well to control the overall performance of the method. The uniform latitude and longitude spacing used in the present study produces smaller cells near the poles; the result is that cells near the poles see fewer satellite paths, and the resulting values of $P_{i,n}$ are lower. Future studies may benefit from using a more equal-area or equal-volume grid representation, such as a geodesic grid[44]. Furthermore, as mentioned in Section II, this study takes the simpler approach of defining the grid in the inertial (J2000) frame, rather than a sun-fixed frame. Expressing the grid in a sun-fixed frame may be useful in some cases, e.g. long-term trending of density model errors that are tied to solar inputs. Additionally, this study has not addressed other ways to solve the linear system in Eq. 45.

The density reconstruction method described in this paper has some practical advantages over existing methods. Unlike a weighted least squares approach where the orbit states and density corrections are estimated simultaneously from tracking data, and where the partial derivatives of the system dynamics and measurements with respect to the state must be found (e.g. see [32]), the tomography method described here requires no such partial derivatives. Note that although the regularization operator (Eq. 45) requires a function to compute the gradient, this gradient is in the estimated density correction $\mathbf{s}$, and is independent of the chosen orbital dynamics, density model, or measurement model. Likewise, no effort needs to be spent on parameterizing the density model corrections to allow them to be easily estimated along with the orbits. For example, Hinks and Psiaki [45] used a unique spline-based density parameterization for another study of density estimation using telemetry from a cross-linked constellation like Iridium. In fact, the tomography method is essentially density-model-agnostic: given a function that describes the modeled density ρ_{mod} in terms of position and time, it is trivial to use this function in the numerical evaluation of the term w that appears in Eq. 15. The main practical constraint on selecting a density model ρ_{mod} is that it should be spatially smooth and capture the major time-varying dynamics, as achieved by most modern empirical and physics-based models.

Furthermore, the tomography problem can be easily scaled to accommodate new data or a different resolution in the solved-for density field. Because the orbit estimates $(\widetilde{\mathbf{r}}_1, \widetilde{\mathbf{v}}_1)$ and $(\widetilde{\mathbf{r}}_2, \widetilde{\mathbf{v}}_2)$ are obtained separately and external to the density estimation, it is straightforward to use orbit estimates generated from different sources. In contrast, a simultaneous estimation scheme that solves for the orbit states and density together must have the raw tracking measurements available: a task that can be challenging when sharing data between organizations. Likewise, it is straightforward to change the desired resolution of the estimated s field by simply changing the grid spacing. This is analogous to using a higher-order spherical harmonic expansion, if one were to use such an expansion to parameterize the density corrections.

A valid argument can be made that the tomography-based density estimation described in this paper should be less accurate than a method that uses raw measurements (e.g. tracking angles) to estimate simultaneously the orbit states and density. The tomography method here represents a nested estimation technique, in which the orbit states are first estimated from measurements, and then these estimated orbit states are treated as measurements in the tomography. In general, an estimation technique using raw measurements will out-perform one using intermediate steps and estimated solutions. This paper also did not address measurement weighting, e.g. if the sensor used at t_1 were of better quality than that used at t_2, or likewise if one satellite had more accurate measurements than another satellite. Thus, a more rigorous evaluation of the tomography method would directly compare the results with those obtained from a simultaneous estimation technique.

VIII. Conclusions

This paper has introduced a new tomography-based method to reconstruct the atmospheric density, which uses the change in specific mechanical energy of satellite orbits as the measurements. This method allows the use of temporally-sparse measurements (e.g. ground-based tracking) to find a time-averaged, yet spatially resolved, global density correction. Because the density corrections are in the form of scale factor adjustments to an assumed density model, it is straightforward to substitute any number of desired density models into the formulation, independent of a specific density parameterization. Based on the simulations performed in this paper, the method requires a number of satellites (~ 50) in spatially diverse orbits and with well-known drag properties (e.g. ballistic coefficient). However, this requirement on the tracking targets is similar in principle to existing methods. These specific simulation results suggest that the time-averaged density over 12 hours can be reconstructed to within approximately 10%.

Appendix A: Error Sensitivity Analysis

This section analyses the errors in the tomography measurements $\Delta\mathcal{E}$ caused by errors in the orbit estimates, and also errors caused by assuming a reference trajectory in the measurement model.

Let the actual measurement $\Delta\mathcal{E}_{\text{meas}}$ be related to an assumed true measurement value $\Delta\mathcal{E}_{\text{true}}$ (i.e. that predicted by a perfect measurement model) along with some measurement error ϵ_{meas}:

$$\Delta\mathcal{E}_{\text{meas}} = \Delta\mathcal{E}_{\text{true}} + \epsilon_{\text{meas}} \; . \tag{49}$$

The measurement error ϵ_{meas} results from errors in the orbit estimation system and the calculation of $\mathbf{r}$ and $\mathbf{v}$ at times t_1 and t_2 using the orbit estimates at those times. Let $\Delta\mathcal{E}_{\text{true}}$ be described by a model $\Delta\mathcal{E}_{\text{model}}$; of course, $\Delta\mathcal{E}_{\text{model}}$ will not be perfect, and this additional error in the form of measurement model error (i.e. process noise), ϵ_{model}, is defined as

$$\epsilon_{\text{model}} \equiv \Delta\mathcal{E}_{\text{true}} - \Delta\mathcal{E}_{\text{model}} \; , \tag{50}$$

thus Eq. 49 becomes

$$\Delta\mathcal{E}_{\text{meas}} = \Delta\mathcal{E}_{\text{model}} + \epsilon_{\text{model}} + \epsilon_{\text{meas}} \; . \tag{51}$$

The error ϵ_{model} from Eq. 50 can then be rewritten using Eq. 16:

$$\epsilon_{\text{model}} = W_{\text{srp}} + W_{\text{d}_{\text{out}}} + \int_{t_{\text{in}}} wsdt - W^*_{\text{srp}} - W^*_{\text{d}_{\text{out}}} - \int_{t_{\text{in}}} w^* sdt \; . \tag{52}$$

where the superscript $(*)$ indicates evaluation on the reference model (i.e. using the reference terms β^*, $\mathbf{r}^*$, and $\mathbf{v}^*$) . The following error terms can then be defined,

$$\delta W_{\text{srp}} \equiv W_{\text{srp}} - W^*_{\text{srp}} \tag{53}$$

$$\delta W_{\text{d}_{\text{out}}} \equiv W_{\text{d}_{\text{out}}} - W^*_{\text{d}_{\text{out}}} \tag{54}$$

$$\int_{t_{\text{in}}} \delta wsdt \equiv \int_{t_{\text{in}}} wsdt - \int_{t_{\text{in}}} w^* sdt = \int_{t_{\text{in}}} (w - w^*) sdt \; , \tag{55}$$

resulting in

$$\epsilon_{\text{model}} = \delta W_{\text{srp}} + \delta W_{\text{d}_{\text{out}}} + \int_{t_{\text{in}}} \delta wsdt \; . \tag{56}$$

The goal of the remainder of this appendix is to show that, for scenarios described in this paper, the numerical values of the terms ϵ_{model} and ϵ_{meas} from Eq. 51 will be small compared with the measured $\Delta\mathcal{E}$ (Figures 3, 4, and 7). Figure 16 shows the absolute value of the error terms from Eqs. 53, 54, and 55 making up ϵ_{model}, evaluated using the truth $(\mathbf{r}, \mathbf{v})$ and reference $(\mathbf{r}^*, \mathbf{v}^*)$ trajectories from the 1000 simulated orbits described in Section VI. The two sets of LEO and higher-eccentricity orbits are visible in these plots. Note that the $\delta W_{\text{d}_{\text{out}}}$ term is zero for the LEO satellites falling entirely within the grid, and hence does not appear in the logarithmic plot in Figure 16. Figure 17 shows the absolute value of the errors δr and δv between the truth and reference orbits at t_2, which gives an indication of how much these trajectories deviate over the 12-hour tomography time span. The following two subsections will individually analyze the two right-most terms in Eq. 56, and compare approximate analytical predictions with the numerical values shown in Figures 16 and 17. As evident in Figure 16, because the term δW_{srp} is several orders of magnitude smaller than the measurement signal (Figure 7), it is not analyzed further.

A. Error in integrated w term

Using Eq. 15, let the term w be written approximately as

$$w \approx -\frac{1}{2} \beta \rho_{\text{mod}} v^3 \tag{57}$$

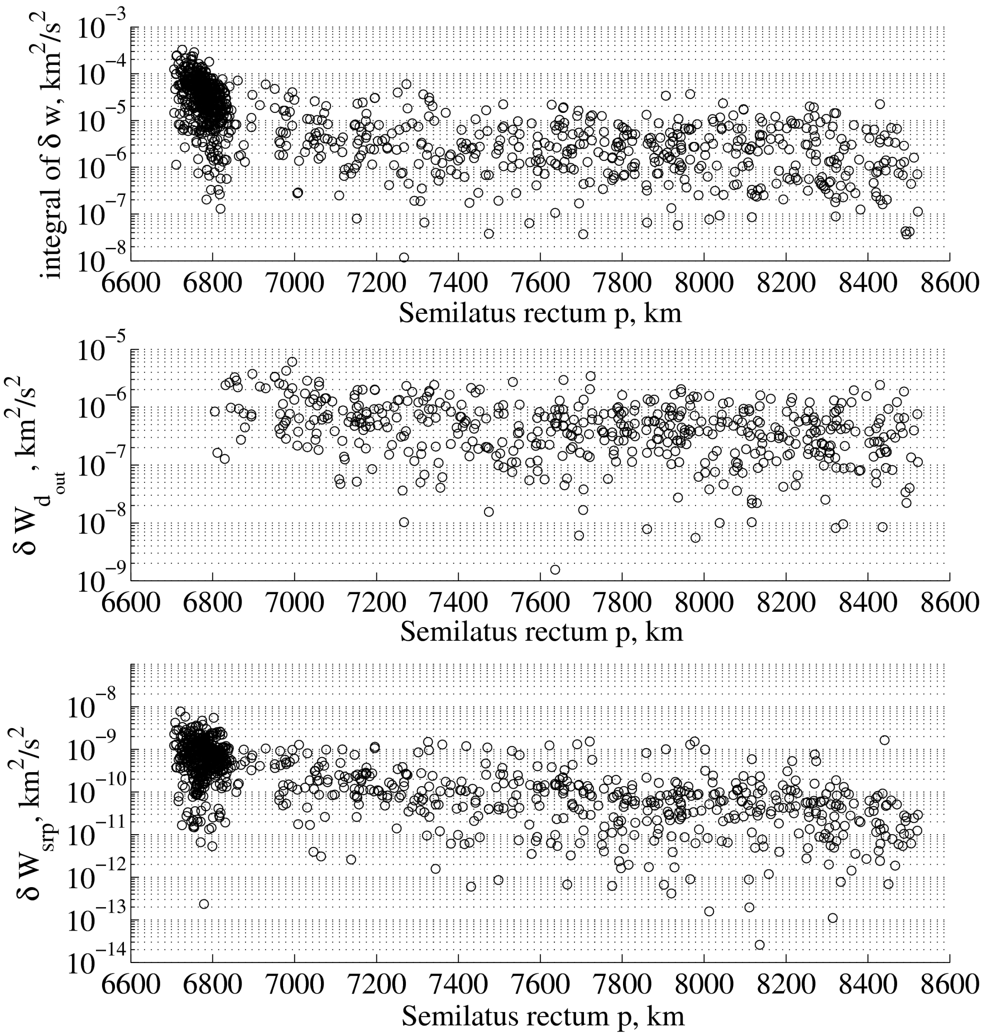

Fig. 16 Absolute value of the error terms making up model error $\epsilon_{\mathrm{model}}$, evaluated from the truth and reference trajectories from 1000 satellite orbits.

(i.e. the effects of a rotating atmosphere are neglected, and the simple exponential density model from Eq. 31 is used), and thus

$$y \approx \int_{t_{\mathrm{in}}} -\frac{1}{2}\beta\rho_{\mathrm{mod}} s v^3 dt \; . \tag{58}$$

From Eq. 55,

$$\int_{t_{\mathrm{in}}} \delta w s dt = \int_{t_{\mathrm{in}}} -\frac{1}{2}\left[\rho_{\mathrm{mod}}(r)\beta v^3 - \rho_{\mathrm{mod}}(r^*)\beta^* v^{*3}\right] s dt \; . \tag{59}$$

One can show that, by linearizing and keeping only first order terms:

$$\rho_{\mathrm{mod}}(r) - \rho_{\mathrm{mod}}(r^*) \approx \frac{\partial \rho}{\partial r}\delta r \tag{60}$$

$$\approx \frac{\delta r}{H}\exp\frac{R - r^*}{H} = \frac{\delta r}{H}\rho_{\mathrm{mod}}(r^*) \tag{61}$$

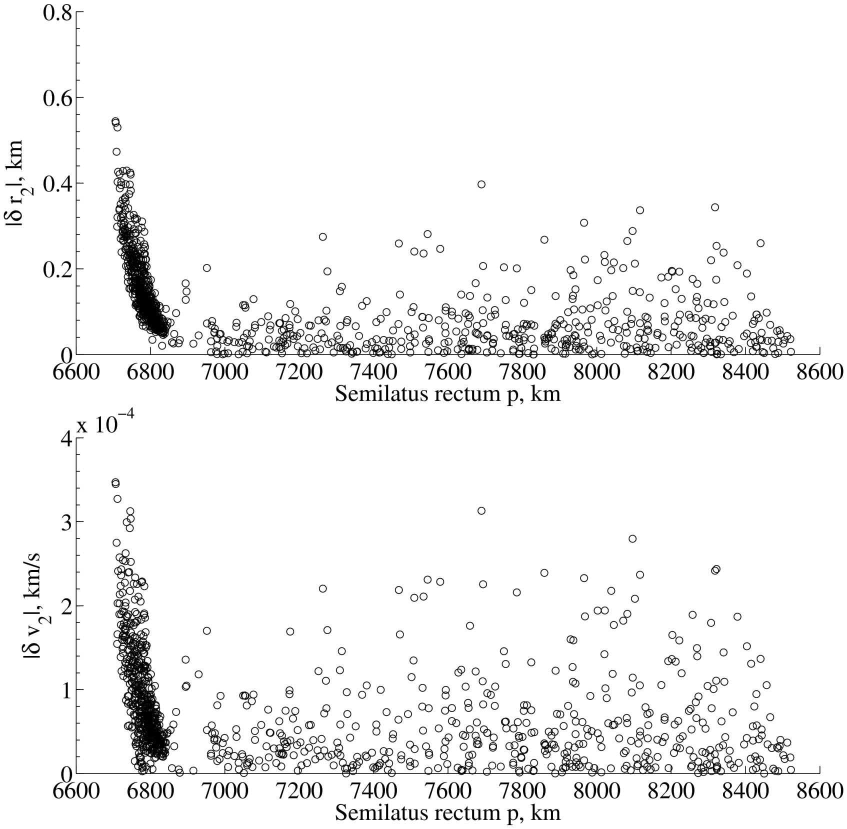

Fig. 17 Absolute value of the errors δr and δv between the truth and reference trajectories at t_2 from 1000 satellite orbits.

keeping in mind that $H = 59.06$ km and $\delta r \sim 0.1$ km (Figure 17), then

$$\rho_{\mathrm{mod}}(r) \approx 0.999\rho_{\mathrm{mod}}(r^*) \tag{62}$$

in other words, $\rho_{\mathrm{mod}}(r)$ and $\rho_{\mathrm{mod}}(r^*)$ will agree to within three decimal places for reasonable values of δr. Likewise, to first order for small δv,

$$v^{*3} = (v + \delta v)^3 \approx v^3 + 3v^2\delta v \tag{63}$$

Because $v \sim 7$ km/s and $\delta v \sim 10^{-4}$ km/s (Figure 17), then the term $3v^2\delta v \sim 10^{-2}$ km/s, which is a small fraction of $v^3 \sim 10^2$ km/s. Hence, $v^{*3} \approx v^3$ for the purpose of this error analysis. After defining $\eta_\beta \equiv \beta^*/\beta$, Eq. 59 becomes

$$\int_{t_{\mathrm{in}}} \delta w s dt \approx \int_{t_{\mathrm{in}}} -\frac{1}{2}\rho_{\mathrm{mod}} s \beta v^3 (1 - \eta_\beta) dt \tag{64}$$

Assuming η_β is approximately constant in time, and recalling Eq. 58,

$$\int_{t_{\mathrm{in}}} \delta w s dt \approx (1 - \eta_\beta) \int_{t_{\mathrm{in}}} -\frac{1}{2}\rho_{\mathrm{mod}} s \beta v^3 dt = (1 - \eta_\beta) y \tag{65}$$

Thus, for sufficiently small δr and δv, the measurement model error due to the integrated δw term will be approximately proportional to the measurement signal y scaled by the fractional error in β^*.

The top subplot of Figure 16 shows the absolute value of the error due to the integrated δw term, evaluated according to Eq. 55. For the set of LEO satellites, the magnitude of this error is around 10^{-4} to 10^{-5} km^2/s^2. Considering that the magnitude of the measurement signal y for these satellites is around 10^{-3} km^2/s^2 (recall Figure 7), then this error is around 1 to 10 percent of the value of the measurement signal. Furthermore, the simulated orbits used 5% (1σ) error in β^* relative to β; hence, using $1-\eta_\beta = 0.05$, then the approximate analytical prediction in Eq. 65 is in agreement.

B. Error in $W_{\mathrm{d_{out}}}$ term

The error in the correction factor for the outside-the-grid drag effects, $\delta W_{\mathrm{d_{out}}}$, follows directly from the result of the previous subsection:

$$\delta W_{\mathrm{d_{out}}} \approx \int_{t_{\mathrm{out}}} \delta w dt \approx (1-\eta_\beta) \int_{t_{\mathrm{out}}} -\frac{1}{2}\rho_{\mathrm{mod}}\beta v^3 dt \tag{66}$$

i.e. the limits of integration now cover the times outside the grid, and $s = 1$ because the density is not a solved-for parameter here. At most, the error term $\delta W_{\mathrm{d_{out}}}$ will be similar in magnitude to Eq. 65. However, considering that the higher-eccentricity orbits are usually chosen such that perigee falls within the grid and apogee falls above the grid, it is likely that $\delta W_{\mathrm{d_{out}}}$ will be small, because it includes the lower-density portions of the atmosphere near apogee. The middle subplot in Figure 16 supports this analysis; the value of $\delta W_{\mathrm{d_{out}}}$ for the higher-eccentricity orbits is around one order of magnitude less than the value of the integrated δw term. Recall that $\delta W_{\mathrm{d_{out}}}$ will be zero for a LEO satellite entirely within the grid.

C. Measurement error ϵ_{meas}

As shown in Fig. 6, the measurement $\Delta\mathcal{E} = \Delta T(\widetilde{\mathbf{v}}_1, \widetilde{\mathbf{v}}_2) + \Delta U(\widetilde{\mathbf{r}}_1, \widetilde{\mathbf{r}}_2)$ is derived from the estimated position and velocity at times t_1 and t_2 according to

$$\Delta\mathcal{E} = \frac{\widetilde{v}_2^2}{2} - \frac{\widetilde{v}_1^2}{2} - \frac{\mu}{\widetilde{r}_2} + \frac{\mu}{\widetilde{r}_1} + \left(U_{\mathrm{pg}}(\widetilde{\mathbf{r}}_2) - U_{\mathrm{pg}}(\widetilde{\mathbf{r}}_1)\right), \tag{67}$$

where $\widetilde{r}_1 = \|\widetilde{\mathbf{r}}_1\|$, $\widetilde{v}_1 = \|\widetilde{\mathbf{v}}_1\|$, and likewise for t_2. The measurement error ϵ_{meas} results from errors between the true and measured orbit states, i.e. recalling Eq. 49,

$$\epsilon_{\mathrm{meas}} = \Delta\mathcal{E}_{\mathrm{meas}} - \Delta\mathcal{E}_{\mathrm{true}} = \Delta\mathcal{E}(\widetilde{\mathbf{r}}_1, \widetilde{\mathbf{v}}_1, \widetilde{\mathbf{r}}_2, \widetilde{\mathbf{v}}_2) - \Delta\mathcal{E}(\mathbf{r}_1, \mathbf{v}_1, \mathbf{r}_2, \mathbf{v}_2). \tag{68}$$

For predicting the approximate variance of ϵ_{meas}, Eq. 67 can be simplified by neglecting the contributions from U_{pg}. If the errors in the measured $\widetilde{r}_1$, $\widetilde{v}_1$, $\widetilde{r}_2$, and $\widetilde{v}_2$ are independent and Guassian, given by the variances σ_{r_1}, σ_{v_1}, σ_{r_2}, and σ_{r_2} respectively, then the variance in the measured change in specific mechanical energy, σ_{meas}, is given by[46]

$$\sigma_{\mathrm{meas}} = \sqrt{\left[\frac{\partial(\Delta\mathcal{E})}{\partial r_1}\sigma_{r_1}\right]^2 + \left[\frac{\partial(\Delta\mathcal{E})}{\partial v_1}\sigma_{v_1}\right]^2 + \left[\frac{\partial(\Delta\mathcal{E})}{\partial r_2}\sigma_{r_2}\right]^2 + \left[\frac{\partial(\Delta\mathcal{E})}{\partial v_2}\sigma_{v_2}\right]^2}, \tag{69}$$

where the superscript tilde is dropped for notational convenience. Without specifying the details of the orbit estimation system, it is reasonable to assume that $\sigma_{r_1} = \sigma_{r_2}$ and $\sigma_{v_1} = \sigma_{v_2}$. Evaluating the partial derivatives of $\Delta\mathcal{E}$ in Eq. 67, where U_{pg} is neglected, and dropping the t_1 and t_2 subscripts on the position and velocity uncertainties results in

$$\sigma_{\mathrm{meas}} = \sqrt{\mu^2\sigma_r^2\left(\frac{1}{r_1^4} + \frac{1}{r_2^4}\right) + \sigma_v^2\left(v_1^2 + v_2^2\right)} \tag{70}$$

Figure 18 shows the absolute value of the measurement error from Eq. 68 from the simulations, and the 3σ uncertainty predicted by Eq. 70. The sinusoidal structure apparent in the predicted variance is caused by the varying position and velocity at different points along an elliptical orbit. For a given elliptical orbit (i.e. value of p), a satellite's position and velocity will depend on true anomaly. Although each satellite is simulated with a time-of-flight of 12 hours, because the simulated satellite orbits used different initial values of true anomaly, the corresponding values of (r_1, v_1) and (r_2, v_2), and hence σ_{meas}, can vary substantially, even for orbits with similar p. Figure 18 confirms that Eq. 70 gives an adequate prediction of the size of the measurement error; for the LEO orbits used for the tomography example, the 3σ boundary is $\approx 5 \times 10^{-5}$ km^2/s^2.

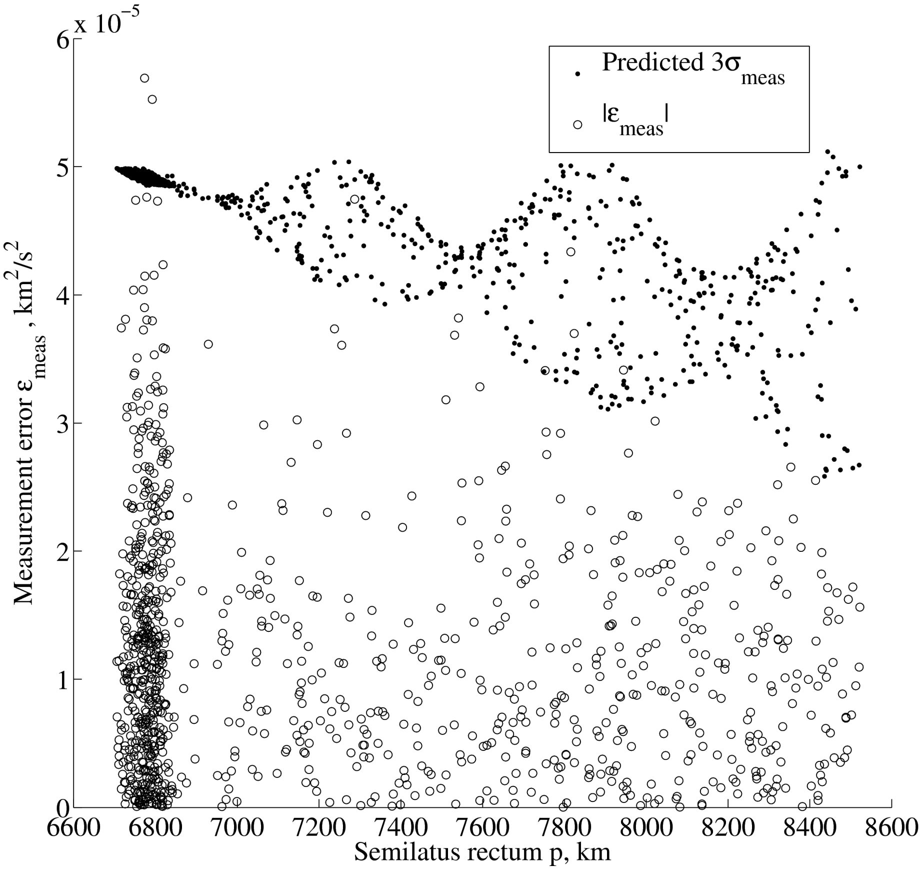

Fig. 18 Error in measured $\Delta\xi$ caused by orbit estimation error, and predicted 3σ variance.

D. Error analysis summary

A convenient way to summarize the error analysis from this section is to show the total error as a fraction of the truth measurement signal, $(\epsilon_{\text{meas}} + \epsilon_{\text{model}})/y$. Figure 19 shows this total fractional error versus $p(t_1)$ for each simulated orbit. A few outliers from the higher-eccentricity orbits (i.e. fractional errors having magnitude greater than 1) have been removed from this plot for clarity. The LEO orbits are shown to have total fractional errors within approximately ± 0.1. This result agrees with the tomography result from Section VI, which obtained reconstructed density accuracies of around 10% using only LEO satellites. Figure 19 also shows that the higher-eccentricity orbits can have worse fractional errors, attributed to the smaller measurement signals y relative to ϵ_{meas}. One way to improve the results for higher-eccentricity orbits is to reduce ϵ_{meas}, e.g. by taking more tracking measurements during orbit estimation. Thus, although the present study has not weighted the measurements $\mathbf{y}$ in the regularization according to the expected measurement uncertainty, the error analysis described here is a useful framework for doing so. These results also provide information for designing the orbit estimation system to deliver the required accuracies on the estimates $(\widetilde{\mathbf{r}}, \widetilde{\mathbf{v}})$ for a required density reconstruction accuracy.

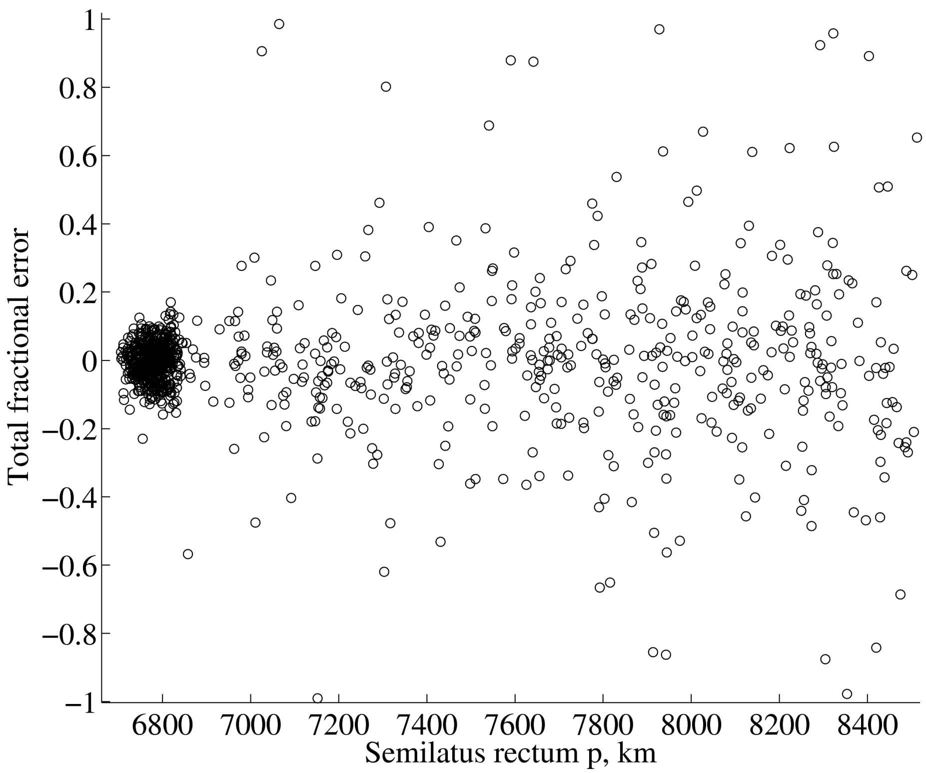

Fig. 19 total fractional error

Acknowledgments

This work was conducted under the auspices of the U.S. Department of Energy, with support from the Los Alamos National Laboratory (LANL) Directed Research and Development program. We thank Humberto Godinez and Andrew Walker of LANL for generating the GITM and NRLMSISE-00 atmospheric density data used in this study. We also thank David Palmer of LANL for valuable discussions leading to the insight regarding the specific mechanical energy of the orbit, and Richard Linares of LANL for valuable inputs regarding measurement error. Finally, we thank the two anonymous reviewers for their careful reading and thoughtful comments on this paper.

References

[1] Marcos, F. A., "Accuracy of atmospheric drag at low satellite altitudes," *Advances in Space Research*, Vol. 10, No. 3, 1990, pp. 417–422, doi:10.1016/0273-1177(90)90381-9.

[2] Vallado, D. and Finkleman, D., "A Critical Assessment of Satellite Drag and Atmospheric Density Modeling," 2010, AIAA Paper 2008-6442, doi:10.2514/6.2008-6442.

[3] Marcos, F. A., Wise, J. O., Kendra, M. J., and Grossbard, N., "Satellite Drag Research: Past, Present and Future," *Advances in the Astronautical Sciences*, edited by J. de Lafontaine, A. J. Treder, M. T. Soyka, and J. A. Sims, Vol. 116, Univelt, Inc., San Diego, CA, 2003, pp. 1865–1878, also, AAS 03-620.

[4] McLaughlin, C. A., Hiatt, A., and Lechtenberg, T., "Precision Orbit Derived Total Density," *Journal of Spacecraft and Rockets*, Vol. 48, No. 1, Jan. 2011, pp. 166–174, doi:10.2514/1.47624.

[5] Doornbos, E. and Klinkrad, H., "Modelling of space weather effects on satellite drag," *Advances in Space Research*, Vol. 37, No. 6, Jan. 2006, pp. 1229–1239, doi:10.1016/j.asr.2005.04.097.

[6] Nicholas, A. C., Picone, J. M., Thonnard, S. E., Meier, R. R., Dymond, K. F., and Drob, D. P., "A methodology for using optimal MSIS parameters retrieved from SSULI data to compute satellite drag on LEO objects," *Journal of Atmospheric and Solar-Terrestrial Physics*, Vol. 62, 2000, pp. 1317–1326, doi:10.1016/S1364-6826(00)00105-X.

[7] Bruinsma, S. and Biancale, R., "Total Densities Derived from Accelerometer Data," *Journal of Spacecraft and Rockets*, Vol. 40, No. 2, 2003, doi:10.2514/2.3937.

[8] Sutton, E. K., Forbes, J., and Nerem, R., "Global thermospheric neutral density and wind response to the severe 2003 geomagnetic storms from CHAMP accelerometer data," *Journal of Geophysical Research*, Vol. 110, No. A9, 2005, pp. 1–10, doi:10.1029/2004JA010985.

[9] Bruinsma, S. L. and Forbes, J. M., "Storm-Time Equatorial Density Enhancements Observed by CHAMP and GRACE," *Journal of Spacecraft and Rockets*, Vol. 44, No. 6, Nov. 2007, pp. 1154–1159, doi:10.2514/1.28134.

[10] Doornbos, E., Den Ijssel, J. V., Luehr, H., Foerster, M., and Koppenwallner, G., "Neutral Density and Crosswind Determination from Arbitrarily Oriented Multiaxis Accelerometers on Satellites," *Journal of Spacecraft and Rockets*, Vol. 47, No. 4, July 2010, pp. 580–589, doi:10.2514/1.48114.

[11] Picone, J. M., Emmert, J. T., and Lean, J. L., "Thermospheric densities derived from spacecraft orbits: Accurate processing of two-line element sets," *Journal of Geophysical Research*, Vol. 110, No. A3, 2005, pp. 1–19, doi:10.1029/2004JA010585.

[12] Emmert, J. T., Picone, J. M., and Meier, R. R., "Thermospheric global average density trends, 1967-2007, derived from orbits of 5000 near-Earth objects," *Geophysical Research Letters*, Vol. 35, No. 5, March 2008, pp. 1–5, doi:10.1029/2007GL032809.

[13] Nazarenko, A. I., Kravchenko, S. N., and Tatevian, S. K., "The Space-Temporal Variations of the Upper Atmosphere Density Derived from Satellite Drag Data," *Advances in Space Research*, Vol. 11, No. 6, 1991, pp. 155–160, doi:10.1016/0273-1177(91)90246-G.

[14] Nazarenko, A., Cefola, P., and Yurasov, V., "Estimating Atmosphere Density Variations to Improve LEO Orbit Prediction Accuracy," *Advances in the Astronautical Sciences*, edited by J. Middour, L. Sackett, L. D'Amario, and D. Byrnes, Vol. 99, Univelt, Inc., San Diego, CA, 1998, pp. 1235–1264, also, AAS 98-190.

[15] Cefola, P., Nazarenko, A., and Yurasov, V., "Refinement of Satellite Ballistic Factors for the Estimation of Atmospheric Density Variations and Improved LEO Orbit Prediction," *Advances in the Astronautical Sciences*, edited by R. Bishop, D. Mackison, R. Culp, and M. Evans, Vol. 102, Univelt, Inc., San Diego, CA, 1999, pp. 1511–1548, also, AAS 99-203.

[16] Cefola, P., Proulx, R., Nazarenko, A., and Yurasov, V., "Atmospheric Density Correction Using Two-Line Element Sets as the Observation Data," *Advances in the Astronautical Sciences*, edited by J. de Lafontaine, A. Treder, M. Soyka, and J. Sims, Vol. 116, Univelt, Inc., San Diego, CA, 2003, pp. 1953–1978, also, AAS 03-626.

[17] Bowman, B. R. and Storz, M. F., "Time Series Analysis of HASDM Thermospheric Temperature and Density Corrections," *AIAA/AAS Astrodynamics Specialist Conference, Aug. 2002, Monterey, CA*, 2002, AIAA Paper 2002-4890, doi:10.2514/6.2002-4890.

[18] Casali, S. J., Barker, W. N., and Bowman, B. R., "Improvements in Density Modeling Using the Air Force Dynamic Calibration Atmosphere Model," *AIAA/AAS Astrodynamics Specialist Conference, Aug. 2006*, 2006, AIAA paper 2006-6168, doi:10.2514/6.2006-6168.

[19] Sutton, E. K., Cable, S. B., Lin, C. S., and Marcos, F. A., "Improved basis functions for dynamic calibration of semi-empirical thermospheric models," *Advanced Maui Optical and Space Surveillance Technologies Conference Paper, Sep. 2011, Maui, Hawaii*, 2011.

[20] Bowman, B. R., "True Satellite Ballistic Coefficient Determination for HASDM," *AIAA/AAS Astrodynamics Specialist Conference, Aug. 2002, Monterey, CA*, 2002, AIAA Paper 2002-4887, doi:10.2514/6.2002-4887.

[21] Storz, M. F., Bowman, B. R., Branson, J. I., Casali, S. J., and Tobiska, W. K., "High accuracy satellite drag model (HASDM)," *Advances in Space Research*, Vol. 36, No. 12, 2005, pp. 2497–2505, doi:10.1016/j.asr.2004.02.020.

[22] Johnson, N. L., "U.S. Space Surveillance," *Advances in Space Research*, Vol. 13, No. 8, Aug. 1993, pp. 5–20, doi:10.1016/0273-1177(93)90563-Q.

[23] Vallado, D. A., *Fundamentals of Astrodynamics and Applications*, Microcosm Press, El Segundo, California, and Kluwer Academic Publishers, Dordrecht, The Netherlands, 3rd ed., 2007.

[24] Santamarina, J. C. and Fratta, D., *Discrete Signals and Inverse Problems: An Introduction for Engineers and Scientists*, chap. 8, John Wiley and Sons, 1st ed., 2005.

[25] Natterer, F., *The Mathematics of Computerized Tomography*, chap. 1, Society of Industrial and Applied Mathematics, Philadelphia, 2001.

[26] Fleming, H., "Satellite Remote Sensing by the Technique of Computed Tomography," *Journal of Applied Meteorology*, Vol. 21, 1982, pp. 1538–1549, doi:10.1175/1520-0450(1982)021<1538:SRSBTT>2.0.CO;2.

[27] Gorbunov, M., "Three-dimensional satellite refractive tomography of the atmosphere : Numerical sim-

ulation," *Radio Science*, Vol. 31, No. 1, 1996, pp. 95–104, doi:10.1029/95RS01353.

[28] Bernhardt, P., Selcher, C., Basu, S., Bust, G., and Reising, S., "Atmospheric Studies with the Tri-Band Beacon Instrument on the COSMIC Constellation," *Journal of Terrestrial, Atmospheric and Oceanic Sciences (TAO)*, Vol. 11, No. 1, 2000, pp. 291–312.

[29] Flores, A., Gradinarsky, L. P., Elosegui, P., Elgered, G., Davis, J., and Rius, A., "Sensing atmospheric structure : Tropospheric tomographic results of the small-scale GPS campaign at the Onsala Space Observatory," *Earth Planets Space*, Vol. 52, No. 1999, 2000, pp. 941–945.

[30] Doicu, A., Trautmann, T. R., and Schreier, F., *Numerical Regularization for Atmospheric Inverse Problems*, chap. 1, Springer-Verlag, 2010, pp. 4 – 8.

[31] Storz, M., "Satellite Drag Accuracy Improvements Estimated From Orbital Energy Dissipation Rates," *Advances in the Astronautical Sciences*, edited by K. Howell, F. Hoots, B. Kaufman, and K. Alfriend, Vol. 103, Univelt, Inc., San Diego, CA, 1999, pp. 1307–1327, also, AAS 99-385.

[32] Storz, M. F., "HASDM Validation Tool Using Energy Dissipation Rates," *AIAA/AAS Astrodynamics Specialist Conference, Aug. 2002, Monterey, CA*, 2002, AIAA Paper 2002-4889, doi:10.2514/6.2002-4889.

[33] Mehta, P. M., Walker, A., McLaughlin, C., and Koller, J., "Comparing Physical Drag Coefficients Computed with Direct Simulation Monte Carlo Using Different Gas-Surface Interaction Models," *Journal of Spacecraft and Rockets*, submitted Dec. 2012.

[34] Walker, A., Mehta, P. M., and Koller, J., "A Quasi-Specular Drag Coefficient Model using the Cercignani-Lampis-Lord Gas-Surface Interaction Model," *Journal of Spacecraft and Rockets*, accepted, 2013.

[35] Aster, R. C., Borchers, B., and Thurber, C. H., *Parameter Estimation and Inverse Problems*, chap. 1, Academic Press, 2011, p. 14.

[36] Schaub, H. and Junkins, J. L., *Analytical Mechanics of Space Systems*, chap. 12, AIAA, 2003, p. 513.

[37] Pisacane, V. and Moore, R., editors, *Fundamentals of Space Systems*, chap. 2, Oxford University Press, 1994, p. 52.

[38] Tikhonov, A. N. and Arsenin, V. Y., *Solutions of Ill-Posed Problems*, Wiley, New York, NY, USA, 1977.

[39] Golub, G. H. and Van Loan, C. F., *Matrix Computations*, Johns Hopkins University Press, 3rd ed., 1996.

[40] Rudin, L., Osher, S. J., and Fatemi, E., "Nonlinear total variation based noise removal algorithms." *Physica D. Nonlinear phenomena*, Vol. 60, No. 1-4, November 1992, pp. 259–268, doi:10.1016/0167-2789(92)90242-f.

[41] Kelecy, T., Shoemaker, M., and Jah, M., "Application of the Constrained Admissible Region Multiple Hypothesis Filter to Initial Orbit Determination of a Break-up," *6th European Conference on Space Debris, Apr. 2013, Darmstadt, Germany*, 2013.

[42] Ridley, A. J., Deng, Y., and Toth, G., "The global ionosphere-thermosphere model," *Journal of Atmospheric and Solar-Terrestrial Physics*, Vol. 68, No. 8, May 2006, pp. 839–864, doi:10.1016/j.jastp.2006.01.008.

[43] Picone, J. M., Hedin, A. E., Drob, D. P., and Aikin, A. C., "NRLMSISE-00 empirical model of the atmosphere: Statistical comparisons and scientific issues," *Journal of Geophysical Research*, Vol. 107, No. A12, 2002, pp. 1468, doi:10.1029/2002JA009430.

[44] Randall, D. A., Ringler, T. D., Heikes, R. P., Jones, P., and Baumgardner, J., "Climate Modeling with Spherical Geodesic Grids," *Computing in Science and Engineering*, Vol. 4, No. 5, 2002, pp. 32–41, doi:10.1109/MCISE.2002.1032427.

[45] Hinks, J. C. and Psiaki, M. L., "Simultaneous Orbit and Atmospheric Density Estimation for a Satellite Constellation," 2010, AIAA Paper 2010-8258, doi:10.2514/6.2010-8258.

[46] Taylor, J. R., *An Introduction to Error Analysis: The Study of Uncertainties in Physical Measurements*, University Science Books, Sausalito, California, 1996, p. 75.